Divergent acute *versus* prolonged *in vivo* GLP-1R responses in β-arrestin 2-deleted primary beta cells

Stavroula Bitsi[1], Yusman Manchanda[1], Liliane ElEid[1], Nimco Mohamed[2], Ben Hansen[2], Kinga Suba[2], Guy A. Rutter[1], Victoria Salem[2], Ben Jones[3] and Alejandra Tomas[1]

[1] Section of Cell Biology and Functional Genomics, Division of Diabetes, Endocrinology and Metabolism, Department of Metabolism, Digestion and Reproduction, Imperial College London, London, UK.

[2] Department of Bioengineering, Imperial College London, London, UK.

[3] Section of Endocrinology and Investigative Medicine, Division of Diabetes, Endocrinology and Metabolism, Department of Metabolism, Digestion and Reproduction, Imperial College London, London, UK.

Abstract

The GLP-1R is a GPCR from the glucagon receptor family with important roles in the regulation of beta cell function and feeding behaviours. After ligand-stimulated G protein binding, active GLP-1Rs are rapidly desensitised by GRKs, followed by recruitment of β-arrestins, scaffolding proteins that terminate G protein interaction through steric hindrance but also act as independent signalling mediators. GLP-1R agonists (GLP-1RAs) are well-established therapeutics in type 2 diabetes and obesity that are nevertheless associated with dose-related gastrointestinal side effects affecting ~50% of patients. Exploiting the power of ligand-directed signalling bias with modified β-arrestin engagement is a promising approach to favour therapeutically beneficial over harmful effects of GLP-1RAs. Although GLP-1R interacts with both β-arrestin isoforms 1 and 2 with similar affinities, expression of the latter is greatly enhanced in beta cells, making this the most functionally relevant isoform. To increase our understanding of the molecular consequences of β-arrestin 2 activity in beta cell GLP-1R function we have assessed *in vivo* glycaemic responses to the pharmacological GLP-1RA exendin-4 in an adult beta cell-specific β-arrestin 2 KO mouse model. KO mice displayed worse exendin-4 responses acutely that then improved after glucose rechallenge 6 hours post-agonist injection, an effect mirrored by differences in plasma insulin levels and in *ex vivo* islet calcium and insulin secretion responses. Similar effects were observed for semaglutide and tirzepatide, two clinically relevant GLP-1RAs, but not for the less β-arrestin 2-reliant biased agonist exendin-phe1. Acute exendin-4-induced cAMP was impaired but cAMP responses to GLP-1 following overnight exendin-4 exposure tended to improve in KO *versus* control islets. Acute signalling defects were attributed to the concerted effect of the phosphodiesterase PDE4 and β-arrestin 1, as beta cell β-arrestin 2 KO islets regained cAMP responsivity with either β-arrestin 1 knockdown or PDE4 inhibition. Cell-cell connectivity was preserved in beta cell β-arrestin 2 KO but lost in control islets imaged *in vivo* following implantation in mouse eyes. While islet GLP-1R internalisation was not affected by β-arrestin 2 KO, both recycling and lysosomal targeting were significantly impaired, with the receptor instead redirected to the TGN. Trafficking results were replicated in INS-1 832/3 β-arrestin 2 knock-down cells, where we also detected increased levels of exendin-4-induced TGN signalling as well as reduced GLP-1R ubiquitination and recruitment of the E3 ubiquitin ligase NEDD4, suggesting a role for this post-translational modification in β-arrestin 2-dependent GLP-1R trafficking. The present study represents the first in-depth *in vivo* and *ex vivo* analysis of the effects of beta cell β-arrestin 2 gene ablation on acute *versus* sustained pharmacological GLP-1R responses.

Introduction

The glucagon-like peptide-1 receptor (GLP-1R), a class B G protein-coupled receptor (GPCR), is a prominent pharmacological target for type 2 diabetes. Binding of endogenous GLP-1 to beta cell GLP-1Rs potentiates postprandial insulin secretion, with pharmacological agonists successfully leveraging this effect to control blood glucose levels in people with type 2 diabetes (Nauck et al., 2021). These agonists are nonetheless associated with side effects such as nausea and diarrhoea, negatively impacting tolerability, and patient quality of life (Bettge et al., 2017). Exploiting pathway selectivity downstream of GLP-1R activation to potentiate the engagement of beneficial over detrimental downstream responses has been proposed as a strategy to reduce side effects and improve adherence (Jones, 2021; Jones et al., 2018; Zhang et al., 2015).

The arrestins, a family of cytosolic adaptor proteins, were first identified as key contributors to GPCR homologous desensitisation, thereby 'arresting' GPCR signalling (Kühn and Wilden, 1987; Lohse et al., 1990). Later research assigned them an additional role as *bona fide* signalling mediators (Luttrell et al., 1999; Luttrell et al., 2001), contributing to the concept of 'biased agonism', whereby either G protein or arrestin-mediated pathways are preferentially activated. In contrast to arrestins 1 and 4, whose expression is confined to the visual system, β-arrestins 1 and 2 (also known as arrestins 2 and 3, respectively) are ubiquitously expressed (Lohse and Hoffmann, 2014). β-arrestins are classically associated with receptor internalisation via clathrin-coated pits (Ferguson et al., 1996; Laporte et al., 2000), however, we and others have shown that they can be dispensable for GLP-1R endocytosis (Buenaventura et al., 2019; Sonoda et al., 2008; Thompson and Kanamarlapudi, 2015). Conversely, there is building evidence that the interaction of GLP-1R and β-arrestin results in autonomous signalling events (Quoyer et al., 2010; Sonoda et al., 2008). Interestingly, GLP-1R pharmacological agonists biased away from β-arrestin recruitment exhibit improvements in signalling duration and capacity for sustained insulin secretion (Jones et al., 2018), while agonist-induced cyclic AMP (cAMP) / protein kinase A (PKA) signalling is prolonged in β-arrestin 1/2 double-knockout (KO) HEK293 cells (Jones et al., 2021), suggesting that β-arrestin deficiency favours sustained GLP-1R action.

The two β-arrestin isoforms result from alternative mRNA splicing (Parruti et al., 1993) and, despite sharing structural and functional similarities, often exhibit differential and at times contrasting actions (Srivastava et al., 2015; van Gastel et al., 2018; Wess, 2022). β-arrestin 2 is additionally much more abundant than β-arrestin 1 in human and mouse pancreatic islets, with ~50-fold increased expression of β-arrestin 2 over 1 in beta cells (Benner et al., 2014; Blodgett et

al., 2015). Whole-body constitutive (Ravier et al., 2014) and beta cell-specific tamoxifen-inducible β-arrestin 2 KO (Zhu et al., 2017) murine models display compromised glucose-stimulated insulin secretion and glucose tolerance, with this phenotype only becoming apparent when the mice are fed a high-fat diet. The latter study attributed these impairments to calcium/calmodulin-dependent protein kinase II (CaMKII)-dependent mechanisms and provided very limited *ex vivo* evidence from beta cell-specific β-arrestin 2 KO islets isolated from lean male mice suggesting that acute GLP-1R agonist-mediated calcium signalling and insulin secretion were not significantly altered (Zhu et al., 2017).

Thus, although knockout studies suggest that the loss of β-arrestin 2 results in deleterious effects on whole body glucose metabolism (particularly under metabolic stress), pharmacological manipulation of GLP-1R agonists away from both β-arrestins 1 and 2 seems to improve their glucose-lowering potency. Additionally, other inconsistencies persist, such as the conflicting effect of β-arrestins on GLP-1R internalisation. Overall, the individual role of β-arrestin 2 in regulating agonist-induced GLP-1R signalling and trafficking in pancreatic beta cells, and the mechanisms involved, remain poorly characterised, particularly *in vivo*.

Given the physiological and pharmacological significance of β-arrestin 2 in beta cell function, we have aimed here to dissect its effects and mechanisms of action on acute *versus* sustained beta cell GLP-1R agonist responses with a range of *in vivo*, *ex vivo* and *in vitro* techniques and models. Our investigations have unveiled a previously unappreciated dual role of β-arrestin 2 in controlling GLP-1R signalling, with an initial potentiating effect in acute responses, present both in primary beta cells and *in vivo*, that then progresses to a dampening effect over prolonged agonist stimulations. We have identified both the cAMP phosphodiesterase PDE4 and β-arrestin 1 as contributing to the acute GLP-1R signalling defect in primary beta cells lacking β-arrestin 2. Finally, we have discovered changes in GLP-1R post-endocytic trafficking and ubiquitination signatures, which correlate with differential recruitment of the E3 ubiquitin ligase NEDD4 to the receptor, a profile that could potentially contribute to the prolonged GLP-1R signalling observed in the absence of β-arrestin 2.

Materials and Methods

Animal studies

All *in vivo* procedures were approved by the UK Home Office under the Animals (Scientific Procedures) Act 1986 (Project Licences PA03F7F0F, P0A6474AE, and PP7151519 to Dr I.

Leclerc, Dr B. Owen, and Dr A. Martinez Sanchez, respectively) and from the local ethical committee (Animal Welfare and Ethics Review Board) at the Central Biological Services unit of Imperial College London. Animals were housed in groups of up to 5 adult mice in individually ventilated cages under controlled conditions (21- 23°C; 12h-light:12h-dark cycles). *Ad libitum* access to standard chow diet was provided. For high-fat, high-sucrose (HFHS) diet studies, animals were put on a 58 kcal % fat and sucrose diet (D12331, Research Diet, New Brunswick, NJ) *ad libitum* for the indicated time periods.

Genomic DNA extraction and genotyping

Genotyping was carried out using ear samples collected from weaned animals. Extraction of genomic DNA was performed in an alkaline lysis buffer (25 mM NaOH, 0.2 mM EDTA pH 8.0 in dH_2O) for 1 hour at 95°C, subsequently neutralised by the addition of 13 mM Tris-HCl, pH 7.4. The genomic DNA was used as a template for a PCR reaction with the appropriate primers (sequences provided in Table 1) and the Phire Green Hot Start II DNA polymerase (F124-L, Thermo Fisher Scientific, MA, USA). The PCR products were visualised on 1-2 % agarose gels using a Bio-Rad ChemiDoc imaging system.

Generation of beta cell-specific β-arrestin 2 KO and control mice

Transgenic mouse models were generated on a C57BL/6 background using the Cre/Lox system. The Pdx1-Cre-ERT (Cre recombinase under the control of the *PDX1* promoter conjugated to a mutant oestrogen receptor sequence) mice were bred in-house, whereas the floxed β-arrestin 2 (Barr2) mice, in which exon 2 is flanked by loxP sites (Barr2 fl/fl), were kindly provided by Professor Marc Caron (Duke University, USA). Pdx1-Cre-ERT mice were crossed with Barr2 fl/fl mice in subsequent breeding pairs until mice hemizygous for the Pdx1-Cre-ERT and homozygous for Barr2 (Barr2 fl/fl) were obtained. These mice were then bred to produce Barr2 fl/fl mice with or without Pdx1-Cre-ERT. Barr2 fl/fl mice injected with tamoxifen were used as a control, since tamoxifen administration is a potential confounder (Hammad et al., 2018; Li et al., 2019). Tamoxifen-treated Pdx1-Cre-ERT mice do not have altered beta cell function compared with wild-type littermates (Fu et al., 2009), thus, they were not used as an additional control. Tamoxifen (T5648, Sigma) dissolved at 20 mg/mL in corn oil (C8267, Sigma) was injected at a dose of 100 mg/kg intraperitoneally (i.p.) at 8 weeks of age for 5 consecutive days to induce Cre recombination and thus, beta cell-specific Barr2 KO mice and littermate controls were generated. Experiments

were conducted at least 10 days after the last tamoxifen injection to allow for a sufficient tamoxifen washout period.

R26-Cre-ERT2 mice were kindly provided by Dr Tristan Rodriguez, Imperial College London, UK. This mouse line allows for ubiquitous tamoxifen-inducible Cre recombination, as a Cre-ERT2 cassette is inserted into the Rosa26 locus. These mice were crossed with Barr2 fl/fl mice until the generation of Barr2 fl/fl mice with or without expression of R26-Cre-ERT2. Tamoxifen administration as described above was used to produce inducible whole-body Barr2 KO and littermate control mice.

Mice that express the genetically encoded calcium indicator GCaMP6f Cre-dependently were used for *in vivo* calcium imaging experiments using islets implanted into the anterior chamber of the eye (Salem et al., 2019). GCaMP6f mice were bred in-house and crossed with Pdx1-Cre-ERT Barr2 fl/fl mice to generate Gcamp6f-Pdx1-Cre-ERT Barr2 fl/+ breeders. Subsequently, Gcamp6f-Pdx1-Cre-ERT Barr2 fl/fl and Gcamp6f-Pdx1-Cre-ERT Barr2 +/+ mice were obtained from the crossings and injected with tamoxifen to yield Gcamp6f+ beta cell Barr2 KO and control Gcamp6f+ Barr2 WT mice, respectively. In this case, the presence of the Cre recombinase is essential for GCaMP6f expression, as the conditional allele contains a loxP-flanked cassette.

Similarly, conditional expression of the biosensor $^{T}EPAC^{VV}$ was utilised for imaging of cAMP dynamics: CAMPER reporter mice (Muntean et al., 2018) were purchased from the Jackson Laboratory (Stock No: 032205) and crossed with Pdx1-Cre-ERT Barr2 fl/fl mice to generate CAMPER-Pdx1-Cre-ERT Barr2 fl/+ breeders. CAMPER-Pdx1-Cre-ERT Barr2 fl/fl and CAMPER-Pdx1-Cre-ERT Barr2 +/+ mice were obtained from the crossings and injected with tamoxifen resulting in CAMPER+ beta cell-specific Barr2 KO and control CAMPER+ Barr2 WT mice, respectively.

Peptides

Peptides were produced by Wuxi AppTec Co. Ltd. (Shanghai, China), using standard solid phase peptide synthesis. Mass spectrometric confirmation of peptide identity and high-performance liquid chromatographic purity assessment were provided by the manufacturer (confirmed >90% purity). Tetramethylrhodamine (TMR)-labelled exendin-4 (exendin-4-TMR) and exendin-9 (exendin-9-TMR) have been described and validated before (Pickford et al., 2020). VivoTag-750 conjugated exendin-4 (exendin-4-VT750), used for optical projection tomography (OPT) imaging,

was synthesised and generously provided by Dr Sebastien Goudreau (ImmuPharma Group, Pessac, France).

Intraperitoneal glucose tolerance tests

Intraperitoneal glucose tolerance tests (IPGTTs) using 2 g/kg glucose were performed immediately and at the indicated time points after agonist injection (co-administered with glucose in the acute test) to examine acute and prolonged glycaemic responses to GLP-1R agonism. The animals were fasted for 2 hours before the tests starting at 8 am the morning of the experiment. Blood samples were analysed at 0, 10, 30, and 60 minutes after glucose ± agonist injection using a Contour glucometer (Bayer) and strips. The food was topped up at the end of the 6-hour IPGTT for agonists with shorter half-life (exendin-4, exendin-phe1, D-Ala^2-GIP) or at the end of each IPGTT for agonists with longer half-life (tirzepatide, semaglutide).

Measurement of insulin secretion in vivo

During selected IPGTTs, blood samples were collected at the indicated time points for plasma insulin analysis. Whole blood samples were collected in potassium EDTA cuvettes (Microvette CB 300, 16.444.100, Sarstedt) and centrifuged at 500 x g for 10 minutes at 4°C. The supernatant (plasma) was collected in fresh Eppendorf tubes and kept at 80°C until analysis with a mouse insulin ELISA kit (ultrasensitive mouse insulin ELISA kit, 90080, Crystal Chem), performed according to the manufacturer's instructions with two technical replicates used per sample.

Alpha and beta cell mass quantification

Pancreata from beta cell β-arrestin 2 KO and control littermates were dissected and fixed in 4% PFA for 24 hours. The tissues were washed twice in PBS and left in 70% ethanol until wax embedding. For each sample, three 5 µm-thick tissue sections separated by 300 µm were stained with guinea pig anti-insulin antibody (undiluted, Dako IR002; Alexa Fluor-488 secondary antibody, Invitrogen) and mouse anti-glucagon antibody (1:500, Sigma-Aldrich G2654; Alexa Fluor-568 secondary antibody, Invitrogen). Images were captured using a widefield Zeiss Axio Observer inverted microscope. Glucagon- and insulin-positive areas were determined as previously described (Johnston et al., 2016) and expressed relative to total pancreas area imaged. The average islet size was approximated by adding the surface of beta cells and alpha cells for each islet per section, calculating the average, and producing the overall average for 3 separate sections per sample. Image J v1.53c was used for image analysis.

Isolation and culture of pancreatic islets

For *ex vivo* islet experiments, pancreatic islets were isolated from appropriate KO and littermate control mice. Pancreata were infused via the common bile duct with RPMI-1640 medium (R8758, Sigma-Aldrich) containing 1 mg/mL collagenase from Clostridium histolyticum (S1745602, Nordmark Biochemicals), dissected, and incubated in a water bath at 37°C for 10 minutes. Islets were subsequently washed and purified using a Histopaque gradient (Histopaque-1119, 11191, Sigma-Aldrich, and Histopaque-1083, 10831, Sigma-Aldrich). Isolated islets were allowed to recover overnight at 37°C in 5% CO_2 in RPMI-1640 supplemented with 10% v/v fetal bovine serum (FBS) (F7524, Sigma-Aldrich) and 1% v/v Penicillin/Streptomycin (P/S) solution (15070-063, Invitrogen).

Implantation of islets in the eye

For chow diet calcium *in vivo* imaging, two 8-week-old female littermates with WT and KO genotypes for β-arrestin-2 (Barr2): one control (Gcamp6f heterozygous, Pdx1-Cre-ERT+ Barr2 +/+) and one KO (Gcamp6f heterozygous, Pdx1-Cre-ERT+ Barr2 fl/fl) were injected with tamoxifen for 5 consecutive days to induce Gcamp6f and Barr2 flox recombination. At 12 weeks of age, the animals were sacrificed, and pancreatic islets isolated. The day after the islet isolation, these were transplanted into the anterior chamber of the eye of six 12-week-old male WT C57BL/6J acceptors. Three of the acceptors received control and three KO donor islets. The success of the implantation was verified after 4 weeks, and imaging experiments carried out 8 weeks after the operation.

Calcium imaging under HFHS diet conditions was carried out as follows: two 8-week-old female littermates with WT and KO genotypes for β-arrestin-2 were concomitantly injected with tamoxifen and introduced to HFHS diet. Diet administration was continued for 8 weeks before animal sacrifice and islet isolation. The islets were implanted in the eyes of three 12-week-old female acceptors that had been on HFHS diet for 4 weeks. The acceptors received KO islets in their left eye and control islets in their right eye. The HFHS diet was continued throughout the study. Imaging experiments were carried out 4-5 weeks after the operation.

In vivo calcium imaging

On the days of the imaging, the acceptor mice for chow diet experiments were injected i.p. with either vehicle (saline) or 10 nmol/kg exendin-4. For HFHS diet experiments, the mice were

injected with 2 g/kg glucose with or without 10 nmol/kg exendin-4. All acceptor mice received both treatments using a cross-over study design with block randomization. Images were captured 30-minutes and 5- or 6-hours post-injection using a Nikon Eclipse Ti microscope with an ORCA-Flash 4.0 camera (Hamamatsu) and Metamorph software (Molecular Devices).

During the imaging experiments, general anaesthesia was induced using isoflurane, and time-lapse confocal microscopy performed using the 488 nm excitation channel for 181 frames with 800 msec exposure per frame. During the chow diet calcium imaging, mice injected with exendin-4 received intraperitoneal injections of 2 g/kg glucose (20% w/v glucose solution) to increase blood glucose levels shortly before image acquisition.

Wave index assignment

Pancreatic beta cells are coupled such that healthy pulsatile insulin secretion is associated with pan-islet calcium oscillations or waves. We defined a wave index to objectively measure the proportion of an islet cross-section involved in calcium oscillatory activity. The wave index of each implanted islet was determined using Fiji: whole-islet mean intensity read-outs were obtained using a manual motion-correction macro developed by Mr. Stephen Rothery [National Heart and Lung Institute (NHLI) Facility for Imaging by Light Microscopy (FILM), Imperial College London]. Next, we determined the average whole islet calcium readout in an image sequence and multiplied this number by 1.2 to determine genuine calcium activity in islets. Using this value, the image sequences were thresholded to select cross-section areas with genuine calcium wave activity, expressed as a percentage relative to the whole islet cross-section area imaged. The highest percentage value in each image sequence was used to determine the islet's wave index for that imaging session. Values were then corrected for the fact that, in implanted islets, approximately 20% of the imaged islet cross-section is covered by blood vessels. Using this method, we were able to determine the presence of four types of calcium wave activity: islets where we observed activity over 0-25% of corrected area were characterized as type 1, if 26-50% of the islet cross-section was active these were typical of type 2, if 51-75% of the cross-section was active islets displayed type 3 activity and lastly, type 4 activity was assigned to islets where 76-100% of the cross-section was active.

Waveform analysis

The wavelength, full width at half-maximum (FWHM), and amplitude was determined for the calcium traces of all islets imaged using MATLAB. Briefly, GCaMP6f fluorescence intensity traces

were normalized to F_{min} and a cut-off value of 1.2 for genuine calcium activity was determined. Peaks in the data were determined using the derivative of the waveform for a given minimum peak height and distance between peaks. Frequency and wavelength were then calculated based upon peak location and value. Amplitude and FWHM were calculated as an average of all individual peak amplitude and FWHM for a given data set. Data without distinct peaking behaviour was discarded as noise.

Connectivity analysis

For single cell connectivity analysis, individual beta cells were identified visually using the negative shadow of nuclei as a guidance for ROI placement. ROIs were subcellular and their XY coordinates and changes in mean intensity were measured. Using a MATLAB script, Pearson R correlation analysis of calcium time traces was performed. Calcium traces were normalised and smoothed using prospective time-points in the dataset. Pearson correlation between individual cell pairs was determined, excluding autocorrelation. An R-value of 0.25 was set as the threshold to signify a connection. Data was resampled using boot strapping to increase accuracy of findings (R-values with $p<0.001$ were deemed statistically significant). R-values were binned as follows: 0.25-0.50, 0.5-0.75 and 0.75-1, and considered to signify weak, medium, or strong connections, respectively. Cartesian line maps showing beta cell connectivity were generated based on cell XY coordinates and connections were assigned yellow, green, or red depending on strength of connections. Heat-map matrices show the R-values for each individual cell pair, with an R-value of 1 assigned for autocorrelation.

Ex vivo calcium imaging

Imaging of whole-islet Ca^{2+} dynamics was performed 24 hours after isolation. Islets from individual animals were pre-incubated for 1 hour in Krebs-Ringer Bicarbonate-HEPES (KRBH) buffer (140 mM NaCl, 3.6 mM KCl, 1.5 mM $CaCl_2$, 0.5 mM $MgSO_4$, 0.5 mM NaH_2PO_4, 2 mM $NaHCO_3$, 10 mM HEPES, saturated with 95% O_2/5% CO_2; pH 7.4) containing 0.1% w/v BSA and 6 mM glucose (KRBH G6), and the Ca^{2+} responsive dye Cal-520, AM (AAT Bioquest). For chow diet experiments, the islets were excited at 488 nm and images captured at 0.5 Hz using a Zeiss Axiovert microscope equipped with a 10X/0.5 numerical aperture objective and a Hamamatsu image-EM camera coupled to a Nipkow spinning-disk head (Yokogawa CSU-10). Volocity Software (PerkinElmer) provided a visualisation interface, while islets were maintained at 37°C on a heated stage constantly perifused with KRBH buffer containing G6 ± 100 nM exendin-4, 11

mM glucose, or 20 mM KCl. For HFHS diet experiments, the islets were imaged with a Zeiss LSM-780 inverted confocal laser-scanning microscope in a 10X objective from the FILM Facility at Imperial College London. Treatments were manually added to the islet dishes by pipetting at the indicated time-points. To ensure that the islets would remain stable, these were pre-encased into Matrigel (356231, Corning) and imaged on glass-bottom dishes. Raw fluorescence intensity traces from whole islet ROIs were extracted using Image J v1.53c. Responses were plotted relative to the average fluorescence intensity per islet during the 6 mM glucose baseline period, before agonist addition.

Islet trafficking experiments

Ex vivo islet trafficking experiments were carried out using intact islets treated in full media in 24-well suspension plates for the indicated time-points. The islets were loaded at the centre of a glass-bottom dish (MatTek, P35G-1.5-10-C) in RPMI without phenol red (32404014, Thermo Fisher Scientific). Z-stacks were obtained by confocal microscopy in a NHLI FILM Zeiss LSM-780 inverted confocal laser-scanning microscope and a 20X objective. The images were analysed using Image J v1.53c and processed using Z project with maximum intensity projections and the mean intensity of selected ROIs was measured.

Ex vivo islet cAMP imaging

CAMPER islet FRET imaging

Intact islets were used 24-48 hours following isolation. 10-20 islets from individual mice were encased into Matrigel on glass-bottom dishes and imaged for fluorescence resonance energy transfer (FRET) between CFP (donor) and YFP (acceptor) with CFP excitation and both CFP and YFP emission settings in a NHLI FILM Zeiss LSM-780 inverted confocal laser-scanning microscope and a 20X objective to capture time-lapse recordings with image acquisition every 6 seconds. The treatments were manually added by pipetting. Specifically, for acute cAMP studies, islets were imaged in KRBH buffer containing 0.1% w/v BSA and 6 mM glucose (KRBH G6) for 1 minute, then exendin-4 at 100 nM was added and imaged for 6 minutes before addition of IBMX at 100 μM for the final 2 minutes of the acquisition. For acute rolipram experiments, islets were captured in KRBH G6 for 1 minute before addition of 100 nM exendin-4, 10 μM rolipram, or a combination of the two for 5 minutes. Finally, for overnight experiments, the islets were incubated in 24-well suspension plates in full media with 1 nM exendin-4 for 16 hours overnight, then washed for 30 minutes in KRBH G6, imaged for 2 minutes in this buffer, then 1 nM GLP-1 was added and

finally, after 4 minutes, 100 μM IBMX was added and imaged for the final 2 minutes of the time-lapse. Raw intensity traces for YFP and CFP fluorescence were extracted from whole islet ROIs using Image J v1.53c and YFP/CFP ratios calculated for each ROI and time-point. Responses were plotted relative to the average fluorescence intensity per islet during the 6 mM glucose baseline period, before agonist addition.

Islet cAMP imaging with cADDis

Islets were infected with cADDis (Green Gi cADDis cAMP Assay Kit, Montana Molecular), a genetically encoded biosensor for cAMP packaged in a BacMam viral vector, following the manufacturer's instructions, 24 hours after isolation. Infected islets were then imaged 24 hours post-infection. Islets were encased into Matrigel on glass-bottom dishes and imaged at 488 nm in a NHLI FILM Zeiss LSM-780 inverted confocal laser-scanning microscope and a 10X objective for time-lapse recordings with image acquisitions every 6 seconds. Treatments were manually added by pipetting. For acute cAMP studies, islets were imaged as above in KRBH buffer containing 0.1% w/v BSA and 6 mM glucose (KRBH G6) for 2 minutes to record the baseline, then exendin-4 at 100 nM was added and islets imaged for 5 minutes before addition of a mixture of 100 μM IBMX and 10 μM forskolin for the final 2 minutes of the acquisition. For overnight experiments, the islets were incubated in 24-well suspension plates in full media with 1 nM exendin-4 for 16 hours overnight, then washed for 30 minutes in KRBH G6, imaged for 2 minutes in this buffer, then 1 nM GLP-1 was added, and islets imaged for 5 minutes and finally, a mixture of 100 μM IBMX and 10 μM forskolin was added and imaged for the final 2 minutes of the acquisition. Raw intensity traces for GFP fluorescence were extracted from whole islet ROIs using Image J v1.53c and mean intensities calculated for each ROI and time-point. Responses were plotted relative to the average fluorescence intensity per islet during the 6 mM glucose baseline period, before agonist addition.

Barr1 siRNA knockdown

For β-arrestin 1 (Barr1) siRNA studies, CAMPER primary mouse islets were dispersed by trituration in 0.05% trypsin/EDTA for 3 minutes at 37°C and seeded at the centre of poly-D-lysine-coated glass-bottom dishes. Dispersed islets were allowed to recover overnight before treatment with Accell mouse Arrb1 (109689) siRNA-SMARTpool (E-040976-00-0005, Horizon Discovery) or non-targeting control siRNA (D-001910-01-05, Horizon Discovery) according to the manufacturer's instructions using the recommended siRNA buffer (B-002000-UB-100, Horizon

Discovery) and serum-free delivery media (B-005000-100, Horizon Discovery). Studies took place 72 hours after siRNA treatment addition.

Islet immunostaining for confocal co-localisation

For immunostaining and fluorescence confocal microscopy, exendin-4-TMR-treated islets were fixed using 4% PFA and stored in PBS. After a 10-minute permeabilisation with PBS containing 0.5 % v/v Triton X-100, the islets were washed once with PBS and incubated in blocking buffer (PBS, 0.1% v/v Tween-20, 1 % w/v goat serum, 1% BSA) for 30 minutes. Primary antibody against Lamp1 (1D4B, Developmental Studies Hybridoma Bank) or TGN38 (2F7.1, MA3-063, ThermoFisher Scientific) in blocking buffer was added overnight, while secondary anti-rat or anti-mouse Alexa Fluor 488 (A-11006, Thermo Fisher Scientific) was incubated for 30 minutes at room temperature. Islets were loaded onto glass-bottom dishes in PBS and z-stacks acquired by confocal microscopy with an Imperial College London NHLI FILM Zeiss LSM-780 inverted confocal laser-scanning microscope and a 63X/1.4 numerical aperture oil immersion objective for Lamp1 and an Imperial College London NHLI FILM Leica Stellaris 8 inverted confocal microscope and a 63X/1.4 numerical aperture oil immersion objective for TGN38. Images were analysed using Image J v1.53c. The Coloc 2 plugin was used for co-localisation analysis from maximum intensity projections.

Optical projection tomography

Whole-body (R26-Cre-ERT2) β-arrestin 2 KO and control mice were injected i.p. with 100 nmol/kg of exendin-4-VivoTag 750 (exendin-4-VT750). After 1 hour or 6 hours, the mice were sacrificed using an overdose of anaesthetic (Euthatal solution for injection, Merial) and transcardially perfused with PBS followed by 4% PFA for perfusion-fixation. The pancreas and brain were dissected, washed once in PBS, and placed in 4% PFA for 1-6 hours. The tissues were subsequently optically cleared using the 3DISCO protocol (Ertürk et al., 2012). Dehydration was achieved by incubating in increasing concentrations (1x 50%, 1x 70%, 1x 80%, 3x 100%) of tetrahydrofuran (401757, Sigma) for 10-16 hours each time. Benzyl ether (108014, Sigma) was subsequently added for 16 hours.

The samples were imaged using an optical projection tomography microscope built by Dr James McGinty and Professor Paul French, Imperial College London. Scripts developed in MATLAB (MathWorks) by Dr McGinty were used for image acquisition, reconstruction, global scaling, and region segmentation. Quantification of object volumes and mean intensity was performed using

3D Objects Counter in Image J v1.53c or mean intensity in Vaa3D software (Allen Institute). 3D images were visualised using Volocity software (Quorum Technologies Inc.).

Cell culture

Cell lines were cultured in humidified incubators at 37°C in 5% CO_2. INS-1 832/3 cells (a gift from Prof Christopher Newgard, Duke University, USA) were grown in RPMI-1640 supplemented with 10% FBS, 1% P/S, 10 mM HEPES (H0887, Sigma), 1 mM sodium pyruvate (11360070, Thermo Fisher Scientific), and 0.05 mM 2-mercaptoethanol (M3148, Sigma). HEK293T cells were maintained in DMEM 4500 mg/L glucose (D6546, Sigma) with 10% FBS and 1% P/S. Cell lines were screened routinely for mycoplasma contamination.

Generation of lentiviral CRISPR vectors and transduction of INS-1 832/3 cells

For knockdown (KD) of β-arrestin 2 in INS-1 832/3 cells, a lentiviral CRISPR approach was utilised. Two guide RNA (gRNA) sequences were cloned using a pScaffold-H1 (118152, Addgene) on a lentiCRISPR v2 backbone (52961, Addgene), using a protocol adapted from (Miguel-Escalada et al., 2019). The gRNA sequences were: 5'-GAAGTCGAGCCCTAACTGCA-3' and 5'- ACCGGTATTTGAAGCCTCTT-3' (reverse complement). The backbone vector was pre-digested with FastDigest Esp3I (FD0454, Thermo Fisher Scientific) for 2 hours at 37°C and purified using Monarch® DNA Gel Extraction Kit (T1020S, New England Biolabs) before digestion-ligation with the gRNA-pScaffold-H1 using FastDigest Esp3I and T7 Ligase (M0318L, New England Biolabs).

To produce lentiviral particles, HEK293T cells were co-transfected with the gRNA lentiviral vector (or the vector without gRNAs - control empty vector), plus the packaging (psPAX2) and envelope (pMD2.G) vectors using a calcium phosphate protocol. Viral supernatants were harvested 48- and 72-hours post-transfection, filtered using a 0.45 µm Millex-HV filter, and concentrated by 20% sucrose gradient ultracentrifugation in an Optima XPN-100 ultracentrifuge at 26,000 rpm at 4°C for 2 hours in a SW32 Ti swinging bucket rotor (Beckman-Coulter). Viral particles were resuspended in PBS and stored at -80°C.

INS-1 832/3 cells were transduced with appropriate amounts of lentiviruses followed by addition of puromycin (4 µg/ml) 72 hours post-transfection. Transduction was performed with the control empty vector (INS-1 832/3 EV) or the vector with gRNAs 1 and 2 (INS-1 832/3 g1-2) to generate β-arrestin 2 KDs. The puromycin was replaced every 2-3 days for a total of 2 weeks to induce the

selection of transduced cells. The surviving selected cells were subsequently cultured in full media in the absence of puromycin and tested for β-arrestin 2 gene expression using qPCR.

Ex vivo insulin secretion assays

Isolated islets used for insulin secretion assays were treated in 24-well non adherent plates. Ten islets were used per well and three technical replicates used per condition. For acute studies, islets were pre-incubated for 1 hour in KRBH buffer (described in *in vitro* calcium imaging) containing 1% w/v BSA (10775835001, Roche) and 3 mM glucose before incubation with 11 mM glucose ± agonists in KRBH in a shaking 37ºC water-bath (80 rpm) for 1 hour. For overnight studies, pre-incubation was carried out in RPMI-1640 media containing FBS, P/S and 3 mM glucose, followed by treatment with media containing 11 mM glucose ± agonists for 16 hours. At the treatment end, supernatants containing the secreted insulin were collected, centrifuged at 1,000 x g for 5 minutes, and transferred to fresh tubes. To determine total insulin content, islets were lysed using acidic ethanol (75% v/v ethanol, 1.5 mM HCl). The lysates were sonicated 3 x 10 seconds in a water bath and centrifuged at 10,000 x g for 10 minutes, and the supernatants collected. The samples were stored at -20ºC until the insulin concentration was determined using an Insulin Ultra-Sensitive Homogeneous Time Resolved Fluorescence (HTRF) Assay kit (62IN2PEG, Cisbio, Codolet, France) according to the manufacturer's instructions. GraphPad Prism 9 was used for the generation of the standard curve and sample concentration extrapolation. The total insulin content was calculated by adding the secreted insulin to the insulin content of the lysates.

HTRF cAMP assays

Intact primary mouse islets were dispersed by trituration in 0.05% trypsin/EDTA for 3 minutes at 37°C. After stimulation, dispersed islets were lysed and cAMP assayed by HTRF immunoassay (cAMP Dynamic 2, 62AM4PEB, Cisbio, Codolet, France).

Transfection of plasmid DNA

Transient transfection of cell lines with plasmid DNA was achieved with Lipofectamine 2000 Transfection Reagent (11668027, Thermo Fisher Scientific) according to the manufacturer's instructions. Briefly, appropriate amounts of DNA were incubated for 5 minutes in Opti-MEM reduced serum medium (31985070, Thermo Fisher Scientific) and gently mixed with an equal volume of Lipofectamine 2000 in Opti-MEM. After 20 minutes, the mix was added dropwise to

cells in culture medium without P/S and incubated for 4-6 hours. The medium was then removed, and full culture medium added. Assays were performed 24 hours or 48 hours post-transfection depending on the experiment.

RNA extraction and qPCR

Samples were lysed in TRIzol Reagent (15596-018, Invitrogen) and briefly vortexed for homogenisation. Phase separation was achieved by chloroform (C2432, Sigma) addition and the upper aqueous phase collected. RNA was recovered by overnight precipitation with isopropanol (11388461, Thermo Fisher Scientific). Following cDNA synthesis using MultiScribe™ Reverse Transcriptase (4311235, Thermo Fisher Scientific) according to the manufacturer's instructions, qPCR was performed using SYBR Green Technology (Fast SYBR Green Master Mix, 4385616, Invitrogen) on an Applied Biosystems™ 7500 Real-Time PCR system. The data was analysed using the $2^{(-\Delta\Delta Ct)}$ method (Livak and Schmittgen, 2001). A list of primer sequences is provided in Table 1.

Table 1. Primers used for genotyping PCR and qPCR

Gene	Species	Forward Sequence (5'→ 3')	Reverse Sequence (5'→ 3')	Application
Barr2 flox	mouse	GAGTCACTGTATGGGTCCCTG	TTGCTGTTCGATGCTACATAACTC	Genotyping
Barr2	mouse	GCGCGACTTTGTAGATCACC	AAGACAGGCCCAGTACATCC	qPCR
Barr2	rat	AAGTCGAGCCCTAACTGCAA	GCCCAGTACATCCAGGTCTT	qPCR
Barr1	rat	TAACGTGCAGTCCTTCCCAC	GAAGGTTTGGCGGGATCTCA	qPCR
Barr1	mouse	CCAGACAGTTCCTTATGTCAGACAA	TTCTCCGTGGTAATAGATCTCCTTATC	qPCR
Beta actin	mouse, rat	CACTGTCGAGTCGCGTCC	TCATCCATGGCGAACTGGTG	qPCR
Pdx1	mouse	CCAAAGCTCACGCGTGGA	TGTTTTCCTCGGGTTCCG	qPCR

CAMPER mut (flox)	mouse	GGTCAGCTTGCCGTAGGTG	GTCCAAGCTGAGCAAAGACC	Genotyping
CAMPER wt (no flox)	mouse	CAGGACAACGCCCACACA	AAGGGAGCTGCAGTGGAGTA	Genotyping
CreERT	mouse	AGCGATGGATTTCCGTCTCT	CACCAGCTTGCATGATCTCC	Genotyping
GCaMP6f mut (flox)	mouse	ACGAGTCGGATCTCCCTTTG	CCGAAAATCTGTGGGAAGTC	Genotyping
GCaMP6f wt (no flox)	mouse	AAGGGAGCTGCAGTGGAGTA	CCGAAAATCTGTGGGAAGTC	Genotyping
Ins1	mouse	GCTGGTGGGCATCCAGTAA	AATGACCTGCTTGCTGATGGT	qPCR
Ins2	mouse	TGGCTTCTTCTACACACCCATGTCCC	ACTGATCTACAATGCCACGCTTCTGCT	qPCR
MafA	mouse	CTTCAGCAAGGAGGAGGTCATC	CGTAGCCGCGGTTCTTGA	qPCR
Kcjn11	mouse	CACGGCGGGATAAGTCTACCT	AATCATTTGCCCCCTTCTTGT	qPCR
Acot7	mouse	AGATGATTGAGGAGGCCGG	ACAGCGCTCCCCATTCTG	qPCR
Ldha	mouse	ATGAAGGACTTGGCGGATGA	ATCTCGCCCTTGAGTTTGTCTT	qPCR
Slc16a1	mouse	GCTTGGTGACCATTGTGGAAT	CCCAGTACGTGTATTTGTAGTCTCCAT	qPCR

Cyclic AMP FRET imaging using global and TGN-targeted $^{T}EPAC^{VV}$

The global $^{T}EPAC^{VV}$ construct was kindly provided by Professor Kees Jalink, the Netherlands Cancer Institute, Netherlands (Klarenbeek et al., 2011). The Trans-Golgi network (TGN)-targeted version was made *in house* by in-frame cloning of the GRIP domain of GolginA1 (pCMV6-KL5-GolginA1, Origene) at the C-terminal end of $^{T}EPAC^{VV}$. INS-1 832/3 EV and g1-2 cells were plated in 48-wells and transfected with 0.5 µg plasmid DNA. After 24 hours, cells were trypsinised and

seeded on glass-bottom dishes. 48 hours post-transfection, cells were imaged in RPMI without phenol red (32404014, Thermo Fisher Scientific) with a NHLI FILM Zeiss LSM-780 inverted confocal laser-scanning microscope using a 20X objective to capture a time-lapse recording of CFP/YFP FRET as described for CAMPER islets with image acquisition every 6 seconds and treatments manually added by pipetting. Cells were imaged for 1 minute to record a baseline, then exendin-4 at 100 nM was added and imaged for 4 minutes before addition of 100 μM IBMX and 10 μM forskolin for the final 2 minutes of acquisition. Raw intensity traces for YFP and CFP fluorescence were extracted from individual cell ROIs using Image J v1.53c and YFP/CFP ratios calculated for each ROI and time-point. Responses were plotted relative to the average fluorescence intensity per islet during the 6 mM glucose baseline period, before agonist addition.

NanoBiT complementation and NanoBRET assays

For Nb37-based bystander complementation assays, the plasmids used were a gift from Prof Asuka Inoue, Tohoku University, Japan (McGlone et al., 2021). Nb37 cDNA (synthesised by GenScript with codon optimisation) was C-terminally fused to SmBiT with a 15-amino-acid flexible linker (GGSGGGGSGGSSSGGG), and the resulting construct referred to as Nb37-SmBiT. The C-terminal KRAS CAAX motif (SSSGGGKKKKKKSKTKCVIM) was N-terminally fused with LgBiT (LgBiT-CAAX). The Endofin FYVE domain (amino-acid region Gln739-Lys806) was C-terminally fused with LgBiT (Endofin-LgBiT). Gαs (human, short isoform), Gβ1 (human), Gγ2 (human), and RIC8B (human, isoform2) plasmids were inserted into pcDNA 3.1 or pCAGGS expression vectors. INS-1 832/3 EV or g1-2 cells were seeded in 6-well plates and co-transfected with 0.2 μg SNAP-GLP-1R or SNAP-GIPR, 0.5 μg Gαs, Gβ1, and Gγ2, 0.1 μg RIC8B, 0.1 μg CAAX-LgBiT or 0.5 μg Endofin-LgBiT with 0.1 μg or 0.5 μg Nb37-SmBiT (1:1 ratio), respectively.

For NanoBRET localisation assays, cells were seeded in 12-well plates and co-transfected with SNAP-GLP-1R-NLuc (generated in-house) and KRAS-, Rab4-, Rab5-, Rab9-, or Rab11-Venus (gifts from Prof Nevin Lambert, Augusta University, USA, and Prof Kevin Pfleger, The University of Western Australia, Australia). For KRAS-, Rab5-, and Rab11-Venus, 0.5 μg were co-transfected with 0.5 μg SNAP-GLP-1R-NLuc, while for Rab4- and Rab9-Venus, 0.25 μg were co-transfected with 0.1 μg SNAP-GLP-1R-NLuc.

24 hours after transfection, cells were detached, resuspended in Nano-Glo® Live Cell Reagent (N2011, Promega) with furimazine (1:20 dilution) and seeded into white 96-well half area plates. Luminescence was recorded at 37°C in a Flexstation 3 plate reader, with total luminescent signal

used for NanoBiT assays and dual wavelength acquisition (460 and 535 nm) for NanoBRET assays. A 5-minute baseline recording was followed by agonist addition and serial measurements over 30 minutes. Readings were taken every 30 seconds and normalised to well baseline and then, average vehicle-induced signal was subtracted to establish the agonist-induced effect. Areas under the curve (AUC) were calculated for each agonist concentration and fitted to four-parameter curves using GraphPad Prism 9.0.

Binding kinetic assay in primary islets

Islets were pre-incubated at 37°C with 1 μM exendin-4 in RPMI-1640 (with FBS and P/S) for 2 hours prior to imaging to saturate receptor binding to generate a negative control for TMR uptake, with exendin-4 maintained for the duration of imaging. These, along with islets not pre-incubated with exendin-4, were incubated with a metabolic inhibitor cocktail (20 mM 2-deoxyglucose, 10 mM NaN_3) to inhibit ATP-dependent endocytosis, as previously described (Fang et al., 2020), for 30 minutes prior to imaging. The metabolic inhibitors were maintained for the duration of the imaging.

Approximately 20 islets were then encased onto Matrigel in glass-bottom dishes and imaged in imaging medium (RPMI-1640 without phenol red, containing metabolic inhibitors) with a Zeiss LSM-780 inverted confocal laser-scanning microscope with a 10X objective from the FILM Facility at Imperial College London. TMR fluorescence was recorded every 2 seconds for 1 minute baseline, followed by 100 nM exendin-4-TMR addition in imaging medium and recording for a further 15 minutes. Curve fitting to an exponential plateau was performed to calculate binding kinetic parameters in Prism 9.0.

Generation of stable SNAP-GLP-1R-expressing beta cell sublines

Five million INS-1 832/3 EV or g1-2 cells were seeded into 10-cm adherent dishes. Each dish was transfected with 9 μg of the SNAP-GLP-1R plasmid (Cisbio) using Lipofectamine 2000 according to the manufacturer's protocol. Forty-eight hours later, 1 mg/mL G418 was added to each dish to select for SNAP-GLP-1R-positive cells. The surviving cells were allowed to proliferate. Once the 10-cm dishes reached >80% confluence, cells were labelled in suspension with SNAP-Surface 549 (New England Biolabs) for 30 minutes at 37°C and FACS-sorted to select for SNAP-GLP-1R-expressing ones. Sorted cells were then cultured and maintained in 1 mg/mL G418 to preserve SNAP-GLP-1R expression.

Immunoprecipitation assays

For NEDD4 co-immunoprecipitation, INS-1 832/3 EV or g1-2 SNAP-GLP-1R cells were transfected with the pCI HA NEDD4 construct (a gift from Prof. Joan Massague, Addgene plasmid #27002) 24 hours before the experiment. Two million INS-1 832/3 EV or g1-2 SNAP-GLP-1R cells were seeded onto cell culture treated 6-well plates and allowed to attach overnight. The next day, the cells were treated with vehicle or 1 μM exendin-4 in RPMI-1640 (containing FBS, P/S and additional HEPES, sodium pyruvate and 2-mercaptoethanol) for 10 minutes at 37°C. Following stimulation, cells were washed 1X in ice-cold PBS and lysed in ice-cold 1X TBS (50 mM Tris-HCl pH 7.4, 150 mM NaCl) supplemented with 1 mM EDTA, 1% Triton X-100, and protease and phosphatase inhibitor cocktails and lysates placed on a rocker for 15 minutes at 4°C. Next, lysates were incubated overnight under rotation at 4°C with ANTI-FLAG® M2 Affinity Gel beads (Merck) to pull down FLAG-containing SNAP-GLP-1R, and pull-downs were performed according to the manufacturer's protocol.

Following the pull-down, the beads were resuspended in 1X TBS and 2X urea loading buffer (20 mM Tris-HCl pH 6.8, 5% SDS, 8 M urea, 100 mM dithiothreitol, 0.02% bromophenol blue) 1:1 and incubated at 37°C for 10 minutes to separate pulled down proteins from beads. Samples were spun at 5000 x g for 30 seconds and the supernatant resolved in acrylamide gels, electroblotted onto polyvinylidene fluoride (PVDF) membranes, incubated with the indicated antibodies and developed as detailed in the Western blotting section. Specific band densities were quantified with Image J v1.53c. The details for the primary antibodies for ubiquitin and HA-tag and respective secondary antibodies are provided in Table 2.

Protein extraction and Western blotting

Protein extraction was performed by lysing samples with Tris/NaCl/EDTA buffer (100 mM NaCl, 50 mM Tris-HCl, 1 mM EDTA, 0.1% BSA, pH 8.6). The samples were sonicated in a water bath sonicator 3X for 10 seconds. 2X urea loading buffer was added 1:1 and samples were incubated at 37°C for 10 minutes before resolving using SDS-PAGE (10% acrylamide gels). Protein transfer to PVDF membranes (Immobilon-P, 0.45 μm pore size, IPVH00010, Merck) was achieved using a wet transfer system (Bio-Rad). The membranes were incubated with appropriate primary and secondary antibodies listed in Table 2 in 5% milk and developed using the Clarity Western enhanced chemiluminescence substrate system (1705060, Bio-Rad) in a Xograph Compact X5 processor. Specific band densities were quantified using Image J v1.53c.

Table 2. Primary and secondary antibodies used for Western blotting									
1º Ab	**Manufacturer**	**Cat. No.**	**Dil.**	**Time, Tº**	**2º Ab**	**Manufacturer**	**Cat. No.**	**Dil.**	**Time, Tº**
ERK 1/2	Cell Signaling Technology	9102S	1:1000	16 h, 4ºC	Rabbit	Abcam	ab205718	1:5000	1 h, RT
pERK1/2	Cell Signaling Technology	9101S	1:1000	16 h, 4ºC	Rabbit	Abcam	ab205718	1:5000	1 h, RT
CREB	Cell Signaling Technology	9197S	1:1000	16 h, 4ºC	Rabbit	Abcam	ab205718	1:5000	1 h, RT
pCREB	Cell Signaling Technology	9198S	1:1000	16 h, 4ºC	Rabbit	Abcam	ab205718	1:5000	1 h, RT
SNAP-tag	New England Biolabs	P9310S	1:500	16 h, 4ºC	Rabbit	Abcam	ab205718	1:5000	1 h, RT
Ubiquitin	Santa Cruz Biotechnology	sc-8017	1:1000	16 h, 4ºC	Mouse	Abcam	Ab6728	1:5000	1 h, RT
HA-tag	Sigma	H3663	1:1000	16 h, 4ºC	Mouse	Abcam	Ab6728	1:5000	1 h, RT

Cell labelling for confocal co-localisation

INS-1 832/3 EV and g1-2 cells transiently expressing the SNAP-GLP-1R were labelled at 37°C with 1 μM of SNAP-Surface 649 fluorescent substrate (S9159S, New England Biolabs) in full media prior to treatment with 100 nM exendin-4 or vehicle for 3 hours. 5 minutes before the end of the latter incubation period, 1 μM LysoTracker Red DND-99 (L7528, Thermo Fisher Scientific) was added. The cells were washed in PBS and fixed in 4% paraformaldehyde, mounted in Prolong Diamond antifade reagent with 4,6- diamidino-2-pM phenylindole (Life Technologies), and imaged by confocal microscopy with an Imperial College London NHLI FILM Zeiss LSM-780 inverted confocal laser-scanning microscope and a 63X/1.4 numerical aperture oil immersion objective

equipped with Zen software (ZEN 2.3 SP1, black, 64-bit, Carl Zeiss). Images were analysed using Image J v1.53c. The Coloc 2 plugin was used for co-localisation analysis.

Time-lapse β-arrestin 2 – GLP-1R co-localisation by spinning disk microscopy

INS-1 832/3 cells stably expressing SNAP-GLP-1R were transiently transfected with a β-arrestin 2-GFP construct. 24 hours after transfection, cells were seeded onto glass bottom MatTek dishes and left to adhere overnight. Cells were labelled in full media with SNAP-Surface 549 (New England Biolabs) for 30 minutes at 37°C and imaged in RPMI without phenol red in a Nikon Eclipse Ti spinning disk confocal microscope with an ORCA-Flash 4.0 camera (Hamamatsu) and Metamorph software (Molecular Devices). Time-lapse images of green and red fluorescence were acquired every 15 seconds for an initial 5-minute baseline prior to addition of 100 nM exendin-4 and further imaging for 10 minutes.

Electron microscopy

Islets extracted from chow diet-fed beta cell β-arrestin 2 KO and control littermates were fixed in EM-grade 2% PFA + 2% glutaraldehyde mix overnight in 0.1 M cacodylate buffer and conventional EM was performed as described (Jones et al., 2018). Briefly, following fixation, islets were post-fixed with osmium tetroxide, encased in 1% agarose, processed for EM, and embedded in Epon resin which was then polymerized at 60°C overnight. 70 nm-thick sections were cut with a diamond knife (DiATOME) in a Leica Ultracut UCT ultramicrotome before examination on an FEI Tecnai T12 Twin TEM. Images were acquired in a charge-coupled device camera (F216, TVIPS), and processed in Image J v1.53c.

Statistical analyses

For single cell connectivity analysis, statistical differences were evaluated using paired or unpaired Student's t-test in MATLAB (MathWorks). All other data analyses and graph generation were performed with GraphPad Prism 9.0. The statistical tests used are indicated in the corresponding figure legends. The number of replicates for comparisons represents biological replicates. Technical replicates within biological replicates were averaged prior to statistical tests.

Data are represented as mean ± SEM, unless otherwise stated. The p-value threshold for statistical significance was set at 0.05.

Results

We first generated a beta cell-specific, tamoxifen-inducible β-arrestin 2 KO mouse model (Fig. 1a, b; Pdx1-Cre-ERT/Barr2 fl/fl mice, and control Barr2 fl/fl mice). β-arrestin 2 gene expression, as determined by qPCR from whole islets (which contain ~80% beta cells), was downregulated by 67% in beta cell β-arrestin 2 KO compared with littermate control mouse islets after tamoxifen induction, while β-arrestin 1 levels were not significantly altered (Fig. 1c). The weight, fasting and fed glycaemia of male or female mice on chow diet did not differ between genotypes (Extended Data Fig. 1a, b). There were also no detectable differences in islet ultrastructure or insulin granule density between genotypes, as assessed by electron microscopy of control and beta cell β-arrestin 2 KO islets (Extended Data Fig. 1c), confirming previously reported data (Zhu et al., 2017).

Noting that anti-hyperglycaemic effects of GLP-1R agonists with bias away from β-arrestin 2 become more prominent later into the dosing window (Jones et al., 2018), we performed intraperitoneal glucose tolerance tests (IPGTTs) acutely and 6 hours after administration of exendin-4 at a range of doses (0.1, 1, and 10 nmol/kg). While we observed no significant effects at either time point for male mice on chow diet (Fig. 1d, e), beta cell β-arrestin 2 KO female mice displayed significantly worse acute glycaemic responses following exendin-4 administration at 1 nmol/kg, but this difference was normalised at 6 hours post-treatment (Fig. 1f), leading to improved ΔAUC (6 hours minus acute) responses when compared with control mice (Fig. 1g). Additional studies in female mice further confirmed the effect of exendin-4 at 1 nmol/kg; this effect was not replicated by administration of the same dose of exendin-phe1, an exendin-4 derivative biased away from β-arrestin 2 recruitment (Jones et al., 2018) and thus, probably, less reliant on the engagement of β-arrestin 2-related mechanisms (Fig. 1h, i).

Additionally, assessment of plasma insulin levels 10 minutes into the IPGTT experiments from above showed that, while there were no significant changes between the two genotypes in exendin-4-treated over vehicle plasma insulin levels in the acute settings, these were significantly raised for beta cell β-arrestin 2 KO *versus* control animals at 6 hours when normalised to their corresponding acute levels (Fig. 1j).

To assess the effect of beta cell-specific β-arrestin 2 deletion on the related glucose-dependent insulinotropic polypeptide receptor (GIPR), we also tested the anti-hyperglycaemic effects of the stable GIPR agonist D-Ala^2-GIP using similar methodology. Although similar trends for improved beta cell β-arrestin 2 KO responses at 6 hours *versus* acutely were observed, they did not reach statistical significance (Extended Data Fig. 1d-g). Additionally, the exendin-4 results were not

replicated in a whole body, tamoxifen-inducible β-arrestin 2 KO model (R26-Cre-ERT2/Barr2 fl/fl), potentially due to compensatory effects exerted by the β-arrestin 2 deletion in different tissues, which, combined, might ablate the phenotype observed in the beta cell-specific model (Extended Data Fig. 1h-k).

To investigate this phenotype in a model of metabolic stress, we administered high-fat high-sucrose (HFHS) diet to both control and beta cell β-arrestin 2 KO mice. Interestingly, KO males gained more weight compared with control littermates after prolonged HFHS diet exposure of more than 10 weeks (Fig. 2a). Additionally, increased beta cell mass and average islet sizes were observed in pancreata from beta cell β-arrestin 2 KO *versus* control animals, with no changes in alpha cell mass and a trend for the ratio of alpha to beta cell mass to be reduced (Extended Data Fig. 2a, b). Study of the levels of expression of beta cell 'enriched' and 'disallowed' genes (Martinez-Sanchez et al., 2015; Pullen et al., 2010) revealed that expression of beta cell 'enriched' genes such as *MafA or Ins2* (with a tendency for the case of *Kcjn11*) was significantly upregulated in KO animals. On the other hand, expression of 'disallowed' genes (*Acot7*, *Slc16a1*, *Ldha*) was not significantly altered (Extended Data Fig. 2c, d).

Fasting glycaemia was elevated in beta cell β-arrestin 2 KO males, but not in females, under HFHS diet, with no changes observed in fed glycaemia between genotypes (Fig. 2b). HFHS-fed KO animals showed worsening of glucose tolerance in an IPGTT compared to control mice (Fig 2c, 2d). However, the glucose-lowering effects of exendin-4 after a glucose challenge persisted more in KO than in control animals 6 hours after agonist injection (Fig. 2c-e), an effect which became highly significant when normalised to their corresponding IPGTT results with vehicle treatment (Fig. 2f). To interrogate the application of the above results to clinically relevant agonists, we performed an analogous study using the long-acting GLP-1R agonist (GLP-1RA) semaglutide and the dual GLP-1R/GIPR agonist tirzepatide [which is known to show reduced β-arrestin recruitment at the GLP-1R but not at its favoured GIPR (Willard et al., 2020)] in HFHS-fed animals. This led to a similar profile of improved responses at 72 hours compared with those at 24 hours post-agonist injection in beta cell β-arrestin 2 KO *versus* control animals (Fig. 2g, h), indicating that lack of β-arrestin 2 might be beneficial for the maintenance of pharmacologically relevant GLP-1R agonist action. Additionally, and as seen for chow diet-fed animals, insulin levels in plasma assessed 10 minutes into the IPGTT experiments from HFHS-fed animals above showed no significant changes between the two genotypes in exendin-4-treated over vehicle conditions in the acute settings, but there was a significant increase in beta cell β-arrestin 2 KO *versus* control animals at 6 hours when normalised to their corresponding acute levels (Fig. 2i).

For insight into the mechanisms underpinning this contrasting acute *versus* prolonged glycaemic responses in beta cell β-arrestin 2 KO animals when compared with control littermates, we undertook further investigations of this phenotype, as well as of the signalling and trafficking profiles of the GLP-1R, in isolated islets. First, to investigate the role of β-arrestin 2 in the modulation of beta cell cAMP dynamics in response to GLP-1R stimulation, we generated a beta cell-specific, tamoxifen-inducible mouse line which conditionally expresses the CAMPER gene, encoding for the cAMP FRET biosensor $^{T}Epac^{VV}$ (Muntean et al., 2018) (Fig. 3a). Time-lapse FRET microscopy experiments in islets isolated from control and beta cell-specific β-arrestin 2 KO CAMPER mice revealed significantly reduced acute cAMP responses to exendin-4 in KO *versus* control animals (Fig. 3b). On the other hand, when islets were pre-treated with 1 nM exendin-4 overnight prior to washing and re-stimulation with GLP-1 to probe the relevance of β-arrestin 2 on GLP-1R de/resensitisation, we found that KO islets tended to produce higher cAMP responses compared with controls, therefore reversing the prior defect in cAMP production detected acutely (Fig. 3c).

The cAMP phenotype was additionally validated in our original mouse model using an HTRF biochemical assay in response to a range of exendin-4 concentrations with dispersed islets isolated from beta cell-specific β-arrestin 2 KO and control animals, and, in agreement with the above results, we detected acute defects in cAMP generation from beta cell β-arrestin 2 KO *versus* control islets, with Emax and LogEC50 parameters either significantly reduced or displaying a tendency for reduction in islets from chow- or HSHS diet-fed animals (Fig. 3d, e). Moreover, we repeated the time-lapse cAMP imaging experiments in islets isolated from beta cell-specific β-arrestin 2 KO and control animals by infecting them with a baculovirus expressing the cAMP Difference Detector in situ (cADDis) biosensor (Tewson et al., 2016), and, again in agreement with our CAMPER results, cADDis-expressing beta cell β-arrestin 2 KO mouse islets displayed a significant defect in acute cAMP generation *versus* control islets (Fig. 3f) but no difference was detected in GLP-1 responses from desensitised islets following overnight exendin-4 pre-incubation (Fig. 3g).

Given the importance of phosphodiesterases in the control of cAMP degradation, and with phosphodiesterase 4 (PDE4) being one of the dominant forms expressed in beta cells (Kilanowska and Ziółkowska, 2020; Pyne and Furman, 2003), we next evaluated the effect of rolipram, a specific inhibitor of PDE4 activity (Zhu et al., 2001), on cAMP generation from beta cell-specific β-arrestin 2 KO and control CAMPER animals. Addition of rolipram normalised the

acute exendin-4-induced cAMP response in KO to that of control islets (Fig. 3h), implicating PDE4 action in the defective beta cell β-arrestin 2 KO acute cAMP phenotype.

We next hypothesised that, as the level of β-arrestin 1 is not reduced in islets from beta cell-specific β-arrestin 2 KO mice (Fig. 1c), and the GLP-1R has been previously shown to also recruit β-arrestin 1 in beta cell lines (Sonoda et al., 2008), compensatory binding of the receptor to this β-arrestin isoform in the absence of the normally most abundant β-arrestin 2 might be responsible for suboptimal cAMP production and/or accumulation. We reasoned that this could potentially result from changes in the degree of GLP-1R acute desensitisation, including, perhaps, differences in the propensity to recruit specific PDE4 isoforms to the receptor between the two β-arrestin isoforms (Perry et al., 2002). To investigate this possibility, we tested the effects of RNAi-mediated β-arrestin 1 knockdown in dispersed (to allow good siRNA access) beta cell β-arrestin 2 KO and control CAMPER islets. Time-lapse FRET imaging experiments did indeed reveal that knockdown of β-arrestin 1 leads to restoration of normal acute cAMP responses to exendin-4 in dispersed beta cell β-arrestin 2 KO CAMPER islets (Fig. 3i), indicating that the previously identified acute cAMP defect in these islets is mediated by compensatory β-arrestin 1 action in the absence of β-arrestin 2.

Calcium has been described as another downstream signalling readout of GLP-1R activation, controlled mainly by Gs but also by Gq protein coupling (Marzook et al., 2021). Intracellular calcium rises are more distal within the GLP-1R signalling pathway compared with cAMP generation and are linked to insulin granule exocytosis. We used the calcium dye Cal520 AM and time-lapse fluorescence microscopy to investigate intracellular calcium dynamics in response to acute exendin-4 treatment in beta cell β-arrestin 2 KO and control islets from either chow-fed or HFHS-fed animals. On chow diet, islets from KO and control animals displayed similar exendin-4-induced calcium rises at 6 mM glucose (Fig. 4a), although response to a subsequent 11 mM glucose challenge was blunted in islets from beta cell β-arrestin 2 KO mice. However, in keeping the observation that HFHS feeding led to accentuation of β-arrestin 2 effects on exendin-4 responses *in vivo*, islets isolated from KO animals on HFHS diet had significantly blunted responses to exendin-4 throughout the acquisition compared to controls (Fig. 4b).

To investigate calcium responses *in vivo*, a mouse model of the genetically encoded calcium indicator GCaMP6f (Chen et al., 2013) was crossed with our β-arrestin 2 KO mice to generate beta cell-specific GCaMP6f β-arrestin 2 KO and WT control mice. Islets from these mice were then isolated and used for implantation in the anterior chamber of the eye of WT acceptor mice.

This platform supported longitudinal *in vivo* imaging of calcium responses as previously shown (Salem et al., 2019). Experiments were carried out under both chow and HFHS diet conditions, with islet donors and islet acceptors matched for diet type. Islet calcium 'waves' in response to treatments were classified in 4 categories of increased 'waving' activity, with category 1 representing the least active and category 4 the most active. In agreement with previous results from diabetic islets (Salem et al., 2019), implanted HFHS-fed mouse islets displayed lower activity compared with their chow diet counterparts (Extended Data Fig. 3a, b). The number of islets examined did not permit for statistical tests, but there was a trend for higher activity indices in HFHS diet islets isolated from beta cell β-arrestin 2 KO compared with control animals. Wave characteristics, such as wavelength, amplitude and full width at half-maximum did not differ between treatments and genotypes for chow diet islets (Extended Data Fig. 3c). For HFHS diet, the amplitude of the calcium waves was significantly increased in beta cell-specific β-arrestin 2 KO *versus* control islets at the 6-hour time-point, both for vehicle and 10 nmol/kg exendin-4 i.p. administrations, while the wavelength and full width at half-maximum parameters were not changed (Extended Data Fig. 3d). The percentage of connectivity of single cells within islets, a measure of coordinated intra-islet responses, was not significantly different between genotypes after exendin-4 administration on chow diet conditions (Extended Data Fig. 3e). However, under HFHS diet conditions, the percentage of connectivity, which initially increased under both genotypes following acute exendin-4 stimulations, then waned over time from 30 minutes to 6 hours post-exendin-4 injection in control islets, but, conversely, a high percentage of connectivity was retained even at 6 hours post-exendin-4 administration in beta cell β-arrestin 2 KO islets (Fig. 4c, d), suggesting that loss of coordinated calcium responses to sustained exendin-4 exposure, present in control conditions, is overcome *in vivo* by the absence of β-arrestin 2.

We next performed *ex vivo* insulin secretion assays from isolated islets, with 1-hour exendin-4 incubations used as acute, and overnight (16-hour, cumulative) incubations as prolonged readouts. Here we observed reduced acute exendin-4-induced insulin secretion (*versus* 11 mM glucose) for beta cell β-arrestin 2 KO mouse islets from animals either on chow or on HFHS diet compared with islets from control animals. However, this effect was reversed overnight, with this temporal trajectory conveniently expressed as "overnight over acute", an effect that was significant for animals on chow diet and close to significance for HFHS diet-fed animals (Fig. 4e, f). Parallel experiments, depicted in the same figure, were performed using the GIPR endogenous agonist GIP, where again we observed the same trend, which, in agreement with our *in vivo* GIP-

D-Ala^2 results, did not quite reach statistical significance, suggesting a lesser dependence of GIPR on β-arrestin 2.

To assess for potential contributions from variations in GLP-1R trafficking to the prolonged exendin-4-induced signalling measured in the absence of β-arrestin 2, we next set out to elucidate GLP-1R trafficking profiles in beta cell β-arrestin 2 KO and control islets using the previously characterised fluorescent agonist exendin-4-TMR (Lucey et al., 2021) as a proxy for endogenous GLP-1R localisation. We started by quantifying the degree of GLP-1R internalisation in response to 1-hour exendin-4-TMR stimulation by measuring TMR fluorescence levels, with acetic acid buffer wash treatment to strip any remaining exendin-4-TMR bound to non-internalised/cell surface receptors, both for chow- and HFHS-fed mouse islets (Fig. 5a). Of note, the acid wash did not significantly reduce TMR signal, indicating that exendin-4-TMR is predominantly internalised under these conditions. We also noted that islets from HFHS-fed mice had generally lower exendin-4-TMR binding capacity than chow-fed mouse islets. We were unable to detect any differences in GLP-1R internalisation between beta cell β-arrestin 2 KO and control islets, suggesting that, as previously observed in cell lines (Buenaventura et al., 2019), β-arrestin 2 does not play a significant role in GLP-1R endocytosis. Next, we assessed the propensity for GLP-1R recycling to the plasma membrane by incubating control or KO islets with exendin-4-TMR for 3 hours after a prior 1-hour incubation with unlabelled exendin-4 to trigger maximal receptor internalisation in both chow- and HFHS diet-fed mouse islets (Fig. 5b). In this assay, re-emergence of agonist-internalised GLP-1R at the cell surface is detected by binding and re-uptake of exendin-4-TMR. While no differences in GLP-1R recycling were detected at the 3-hour time-point for chow diet mouse islets, HFHS KO islets displayed a small but significant reduction in GLP-1R recycling following exendin-4 stimulation. We next repeated the recycling assay in chow diet-fed mouse islets for 6 hours of receptor recycling to assess any possible changes that might only become apparent within longer periods (Fig. 5c). Under these conditions, a small but significant reduction in GLP-1R recycling became apparent in chow diet-fed mouse beta cell β-arrestin 2 KO *versus* control islets.

To control for differences in GLP-1R intracellular localisation potentially due to different levels of receptor expression at the cell surface in basal conditions, we quantified surface GLP-1R levels in control and beta cell β-arrestin 2 KO islets by labelling them with the fluorescent antagonist exendin-9-TMR (Fig. 5d). No differences were observed in the level of basal surface GLP-1R level between the two genotypes. We next assessed the level of co-localisation between exendin-4-TMR and LAMP1, a marker for the lysosome, as well as TGN38, a marker for the trans-Golgi

network (TGN), in islets fixed after 3 hours of exendin-4-TMR stimulation (Fig. 5e, f). We found significantly reduced co-localisation levels between the fluorescent exendin and LAMP1, as well as significantly increased exendin-4-TMR co-localisation with TGN38, in beta cell β-arrestin 2 KO *versus* control islets, suggesting a reduced capacity for GLP-1R trafficking to lysosomal compartments and an increased propensity for redirection to the TGN in the absence of β-arrestin 2.

Next, to assess *in vivo* GLP-1R agonist accumulation within the pancreas following exendin-4 exposure, we performed 3D optical projection tomography (OPT) imaging and signal quantification from optically cleared whole pancreata extracted from global β-arrestin 2 KO or control mice previously injected with the near infrared exendin-4 derivative exendin-4-VivoTag 750 either 1 hour or 6 hours prior to intracardial fixation and pancreas extraction (Extended Data Fig. 4a, b). Results showed a significant loss of signal from control mice pancreata at the 6-hour over the 1-hour period, while signal was instead maintained in β-arrestin 2 KO mice samples.

Finally, we also evaluated the capacity for the GLP-1R to bind to 100 nM exendin-4-TMR in the presence and absence of β-arrestin 2 in islets isolated from beta cell-specific β-arrestin 2 KO *versus* control mice imaged by time-lapse confocal microscopy in the presence of metabolic inhibitors to inhibit receptor endocytosis (Fig. 5g). Fitted curve results showed that, while kinetic parameters [maximum value (YM) and rate constant (k)] were not altered, there is a significant reduction in the binding AUC for beta cell β-arrestin 2 KO when compared with control islets, indicating the existence of a defect in GLP-1R exendin-4-TMR binding capacity in beta cells lacking β-arrestin 2, a phenotype that could contribute to the observed deficit in acute GLP-1R signalling from these islets.

After characterisation of GLP-1R responses in the adult beta cell β-arrestin 2 KO mouse model, we next generated an *in vitro* beta cell model for a more detailed examination of the molecular mechanisms associated with the changes observed in receptor trafficking and signalling *in vivo* and in primary islets. We first verified the pattern of recruitment of β-arrestin 2 to the plasma membrane following GLP-1R stimulation in our chosen model, namely the INS-1 832/3 rat insulinoma cell line (Extended Data Fig. 5a, b). Time-lapse spinning disk microscopy experiments performed in INS-1 832/3 stably expressing SNAP-GLP-1R and transiently transfected with a β-arrestin 2-GFP construct demonstrated that β-arrestin 2 is recruited from the cytoplasm to the plasma membrane where it co-localises with the SNAP-tagged GLP-1R within 5 minutes of stimulation with 100 nM exendin-4.

Next, we generated a lentiviral CRISPR/Cas9-derived INS-1 832/3 cell line in which the β-arrestin 2 gene was ablated. The resulting INS-1 832/3 β-arrestin 2 knockdown (KD) cells displayed a 51% reduction in the level of β-arrestin 2 expression compared with control cells generated in parallel with a non-targeting CRISPR/Cas9 lentivirus (Fig. 6a). Using this cell model, we first assessed the degree of GLP-1R plasma membrane and endosomal signalling by implementing a NanoBiT assay based on the Nb37 (McGlone et al., 2021), a nanobody which specifically binds to active Gs proteins following GPCR stimulation (Irannejad et al., 2013). In agreement with our previously detected acute cAMP defect in beta cell β-arrestin 2 KO islets, this experiment revealed a small but significant reduction in Emax, with no change in logEC50, for exendin-4-induced GLP-1R signalling at the plasma membrane in β-arrestin 2 KD compared with control cells, with no changes associated with the degree of endosomal signalling (Fig. 6b, c). A similar experiment performed with the GIPR agonist D-Ala^2-GIP did not reveal any significant changes in GIPR plasma membrane or endosomal signalling in the β-arrestin 2 KD *versus* control cells (Extended Data Fig. 6a, b).

Following up on our *ex vivo* trafficking results showing reduced GLP-1R targeting to lysosomal compartments but increased trafficking to the TGN in β-arrestin 2 KO islets, we next assessed the level of signalling specifically from this latter intracellular compartment with time-lapse FRET analysis using a cAMP ^{T}Epac^{VV}-based biosensor modified *in house* to localise specifically to the TGN (Fig. 6d). Quantification of cAMP production after exendin-4 stimulation with both global (cytoplasmic) and TGN-targeted ^{T}Epac^{VV} biosensors demonstrated a significant increase in TGN over global cAMP in β-arrestin 2 KD *versus* control cells (Fig. 6e, f). Signal transmission was next assessed by Western blot analysis of the level of ERK1/2 and CREB phosphorylation using phospho-specific antibodies in both control and β-arrestin 2 KD cells at different times of exendin-4 exposure. Results indicate increased basal levels of phospho-ERK1/2 (and a similar trend for increased basal phospho-CREB) but reduced ERK1/2 and CREB phosphorylation fold increases at 5 minutes post-exendin-4 stimulation in β-arrestin 2 KD *versus* control cells (Fig. 6g-i).

We next evaluated the basal levels of endogenous GLP-1R expression at the cell surface in both cell lines by labelling with the fluorescent GLP-1R antagonist exendin-9-TMR and, as for primary islets, we found no difference in cell surface GLP-1R levels between control and β-arrestin 2 KD INS-1 832/3 cells (Fig. 7a). We then performed a comprehensive assessment of GLP-1R trafficking in these cells by using NanoBRET subcellular localisation assays based on the expression of specific Rab GTPase bystanders at different intracellular locations (Fig. 7b). These experiments revealed no differences in GLP-1R internalisation or Rab5-positive endosomal

localisation in response to increasing concentrations of exendin-4 between both cell types. However, in agreement with our previous recycling results in primary islets, there was a clear decrease in GLP-1R localisation to Rab11-positive recycling endosomes, associated with reduced Emax, in cells with reduced β-arrestin 2 levels compared with controls (Fig. 7c, d). We also investigated if there were any differences associated with GLP-1R localisation to either Rab4- or Rab9-positive compartments, corresponding to a fast recycling route and to the retrograde endosome-to-Golgi transport, respectively, and, although we found no effect on receptor localisation to Rab4-endosomes, we measured significantly increased GLP-1R recruitment to Rab9-positive compartments in β-arrestin 2 KD cells (Fig. 7e), suggesting that these cells recapitulate the trafficking phenotype obtained with beta cell β-arrestin 2 KO primary islets, where GLP-1R re-routing to the TGN is observed. We also performed GLP-1R lysosomal localisation studies in INS-1 832/3 control and β-arrestin 2 KD cells transiently expressing a SNAP-tagged GLP-1R labelled with a fluorescent SNAP-Surface probe and Lysotracker under vehicle and exendin-4-stimulated conditions (Fig. 7f, g), and, as seen for islets, found significantly reduced lysosomal localisation of exendin-4-stimulated GLP-1Rs in β-arrestin 2 KD *versus* control cells.

Finally, we investigated the degree of GLP-1R ubiquitination as a possible mechanism that might underlie the post-endocytic trafficking differences observed between β-arrestin 2 KD and control cells. To this effect, we performed immunoprecipitation experiments in control and β-arrestin 2 KD INS-1 832/3 cells modified to stably express SNAP-GLP-1Rs (Fig. 7h, i). Results in control cells surprisingly showed that the GLP-1R is constitutively ubiquitinated in vehicle conditions and undergoes partial deubiquitination following exendin-4 stimulation. They also revealed a significant reduction in the degree of GLP-1R ubiquitination in β-arrestin 2 KD cells, evident already under vehicle conditions. We have previously identified, in an RNAi screen for factors involved in regulating exendin-4-stimulated insulin secretion (Buenaventura et al., 2018), the E3 ubiquitin ligase NEDD4 (neural precursor cell expressed, developmentally downregulated-4), best known to mediate β-arrestin 2-dependent ubiquitination and endo-lysosomal sorting of GPCRs following ligand stimulation (Dores and Trejo, 2019; Wang et al., 2020), as a factor whose downregulation results in a reduction in exendin-4-stimulated insulin secretion in beta cells. More recently, we have also identified NEDD4 as a GLP-1R interactor in a mass spectrometry analysis of the receptor beta cell interactome (unpublished results). We hence next analysed whether the changes in GLP-1R ubiquitination observed in cells with reduced β-arrestin 2 levels could be attributed to variations in the level of recruitment of this ubiquitin ligase to the receptor. To test this hypothesis, we co-immunoprecipitated NEDD4 with the receptor from control and β-arrestin

2 KD INS-1 832/3 cells stably expressing SNAP-GLP-1R and previously transfected with an HA-tagged NEDD4 construct to quantify the level of HA-NEDD4 associated with the GLP-1R (Fig. 7j, k). Results for NEDD4-GLP-1R interaction closely replicated those found for ubiquitination, in that the GLP-1R was found constitutively associated with NEDD4, with GLP-1R-NEDD4 interaction partially lost following exendin-4 stimulation in control cells. Furthermore, the level of GLP-1R-associated NEDD4 was significantly reduced in β-arrestin 2 KD *versus* control cells, a phenotype that, as for ubiquitination, was already present under vehicle conditions.

Discussion

This study builds upon our previous data in cell lines indicating the existence of GLP-1R signalling alterations resulting from β-arrestin 2 downregulation (Jones et al., 2021). To date, there was very limited data available on primary islets and none *in vivo* for the potential role of this important signalling regulator in the modulation of GLP-1R responses, despite the known capacity of biased GLP-1R agonists with differential G protein over β-arrestin recruitment propensities to modify beta cell behaviours (Jones et al., 2018; Zhang et al., 2015). Besides, previously reported experiments showing no apparent effect of adult beta cell β-arrestin 2 deletion on GLP-1R responses had been performed acutely in islets from male mice under chow diet (Zhu et al., 2017), a condition where, in consonance, we also failed to detect any significant effects *in vivo*. After performing careful assessments, however, we were able to establish a clear phenotype in female mice, as well as in both male and female mice fed a HFHS diet over 16 weeks, unveiling an acute signalling defect that evolved towards a prolonged improvement of *in vivo* exendin-4 responses over longer stimulation periods in adult beta cell β-arrestin 2-deleted animals. While the reasons behind the observed sex dimorphism for β-arrestin 2 dependency of GLP-1R responses have not been elucidated here, it is of note that the improved prolonged over acute effects of the lack of β-arrestin 2 are not seen in males, which are well known (and also observed here in the HFHS experiment under vehicle conditions) to display increased diet susceptibility to impaired glucose metabolism and type 2 diabetes (Tramunt et al., 2020), opening the door to potential sex differences in beta cell GLP-1R responses, as previously detected for glucose-stimulated GLP-1 secretion (Faerch et al., 2015).

The validity of the *in vivo* data presented here is reinforced by our observations of concomitant increases in sustained over acute plasma insulin levels from beta cell β-arrestin 2 KO *versus* control mice, as well as by the loss of effect when using exendin-phe1, an exendin-4-derived GLP-1RA with a single amino acid N-terminal substitution biased away from β-arrestin recruitment

(Jones et al., 2018), a feature that likely allows it to bypass both the positive and the negative effects of β-arrestin 2 for its *in vivo* responses. Moreover, the pharmacological relevance of our observations was clearly established by the fact that the currently leading, as well as the most promising GLP-1RAs, namely semaglutide and tirzepatide (Frias et al., 2021), both elicit similar responses to exendin-4 in beta cell β-arrestin 2 deleted *versus* control mice. Interestingly, however, we could not replicate the above-mentioned *in vivo* phenotype when using a whole animal β-arrestin 2 KO model, suggesting that β-arrestin 2 modulation of GLP-1R action in beta cells is compensated by concomitant changes in this or other receptor responses within other tissues, resulting in a zero net effect in glucose handling. Additionally, while the effect of knocking out beta cell β-arrestin 2 on endogenous islet responses has not been extensively characterised here, we have nevertheless found, in agreement with previously published data (Zhu et al., 2017), a significant glucoregulatory defect in HFHS diet-fed mice under vehicle conditions, suggesting a negative impact of absence of β-arrestin 2 on general beta cell function, which, in our study, was also accompanied by increases in beta cell mass and average islet sizes, as well as by increased expression of beta cell 'enriched' genes, indicating lack of receptor signalling control and greater beta cell hypertrophy under metabolic stress in cells lacking β-arrestin 2.

We have here additionally performed a comprehensive *ex vivo* study of the consequences of deleting β-arrestin 2 from beta cells on GLP-1R downstream signalling responses, revealing an acute defect in cAMP production by three separate methods, that is subsequently overcome when probing for the degree of receptor desensitisation after sustained agonist exposure. Moreover, we determined the involvement of the cAMP phosphodiesterase PDE4 and the β-arrestin 1 isoform on the establishment of this acute defect, as cAMP production was restored in islets treated with the PDE4-specific inhibitor rolipram or following siRNA-mediated β-arrestin 1 knockdown. These two effects might be functionally linked, so that increased β-arrestin 1 recruitment could potentially be responsible both for a higher level of acute homologous receptor desensitisation as well as for the augmented recruitment of PDE4 in the absence of β-arrestin 2, as it is known that β-arrestins can desensitize GPCRs not solely by dampening the rate of cAMP generation, but also by increasing the local rate of cAMP degradation following β-arrestin-mediated recruitment of specific PDE isoforms (Baillie et al., 2003; Perry et al., 2002; Willis and Baillie, 2014). Additionally, we observed a concomitant reduction in acute exendin-4-TMR binding to the GLP-1R in primary islets lacking beta cell β-arrestin 2: this could again represent a difference in behaviour between both arrestin isoforms, as β-arrestin 2 is known to induce receptor conformations with higher agonist-binding affinity than β-arrestin 1 for certain GPCRs (Saleh et

al., 2017; Sanni et al., 2010). Overall, our results indicate that the design of biased GLP-1R agonists away from recruitment of both β-arrestin isoforms should be favoured to elicit enhanced sustained GLP-1R responses without triggering acute deficits.

In the present study, we also show that the observed reduction in acute GLP-1R cAMP production is propagated towards acute deficits in calcium responses and insulin secretion from beta cell β-arrestin 2 KO islets, an effect that is eventually overcome during sustained exendin-4 stimulation periods, so that the net effect is increased sustained *versus* acute calcium and insulin responses in islets with beta cell deleted β-arrestin 2. Moreover, our *in vivo* beta cell connectivity analysis has unveiled that the acute rise in connectivity triggered by GLP-1R agonism, previously observed in a separate study (Hodson et al., 2013), is only sustained over time following deletion of β-arrestin 2 under conditions of metabolic stress triggered by prolonged HFHS feeding, suggesting that GLP-1RAs biased away from β-arrestin recruitment might also trigger similar long-term improvements in islet connectivity.

To further our knowledge of the molecular mechanisms underlying the prolonged benefits of beta cell β-arrestin 2 absence, we have also assessed here islet GLP-1R trafficking patterns and found no differences in GLP-1R cell surface or internalisation levels in beta cell β-arrestin 2 KO islets, as previously observed by our group using cell lines, and reminiscent of the behaviour of the closely related GIPR in β-arrestin 2 knocked-down adipocytes (Abdullah et al., 2016). There was however a significant reduction in active GLP-1Rs targeted to lysosomal compartments, accompanied by concomitant reductions in receptor plasma membrane recycling and a redirection of stimulated receptors to the TGN in islets with beta cell-deleted β-arrestin 2. These results were unexpected, as they are opposite to those found in the above-mentioned study of GIPR trafficking in β-arrestin 2 knocked-down adipocytes (Abdullah et al., 2016), and those triggered by the GLP-1R biased compound exendin-phe1, which is associated with reduced recruitment of both β-arrestin isoforms to the receptor, and triggers enhanced instead of reduced GLP-1R plasma membrane recycling together with reduced lysosomal degradation (Jones et al., 2018). Overall, our results suggest that in the absence of just β-arrestin 2, binding of the receptor to the remaining β-arrestin 1 isoform might result in a different trafficking effect than with reductions in binding to both arrestins triggered by G protein biased GLP-1RAs.

Additionally, using an *in vivo* technique involving the injection of the near infrared labelled exendin-4 derivative Ex-4-VT750, we were able to measure a significant loss of signal in cleared pancreata extracted from control animals at 6-hours over 1-hour post-agonist injection that was

no longer present in pancreata from β-arrestin 2 KO mice, suggesting potentially increased maintenance of pancreatic GLP-1R levels over prolonged stimulation periods in the absence of β-arrestin 2, in agreement with our detected reduction in GLP-1R lysosomal targeting, and hence presumably, degradation.

Most of the observations from this study are from *in vivo* or *ex vivo* experiments in islets, but we have nevertheless also created a rat insulinoma cell model with CRISPR/Cas9 deleted β-arrestin 2 expression to test our signalling and trafficking hypotheses in further detail. Using these cells, we have been able to confirm that β-arrestin 2 downregulation triggers reduced GLP-1R plasma membrane signalling efficacy without any loss in endosomal signalling, a phenotype that is accompanied by increased basal levels but reduced acute (5-minute) phospho-ERK1/2 and phospho-CREB fold increases following exendin-4 stimulation. Furthermore, in agreement with our previous results from islets, we have also observed reduced targeting of active GLP-1Rs to both recycling endosomes and lysosomes but increased interaction with the endosome-to-TGN marker Rab9 together with increased TGN over global cAMP production, suggesting that, as seen before for other GPCRs (Godbole et al., 2017), GLP-1Rs rerouted to the TGN in the absence of β-arrestin 2 are able to signal from this intracellular location.

In parallel to our study of GLP-1R behaviours, we have also performed a limited number of experiments on the effect of beta cell β-arrestin 2 deletion on GIPR responses. Despite similar *in vivo* tendencies towards reduced sustained over acute glucose levels in both male and female beta cell β-arrestin 2 KO animals treated with the stable GIP analogue D-Ala^2-GIP, these did not reach statistical significance, suggesting a reduced effect of β-arrestin 2 on this receptor compared with the GLP-1R. Accordingly, acute insulin secretion in response to GIP only showed a tendency towards reduction in beta cell β-arrestin 2 KO islets from chow diet-fed animals, although it did reach significance for mice fed a HFHS diet, and the same tendency towards sustained improvements than for the GLP-1R. Also in agreement, no differences in plasma membrane or endosomal signalling were detected in β-arrestin 2 knockdown rat insulinoma cells stimulated with GIP.

Finally, and as β-arrestin 2 has previously been found to be required for E3 ubiquitin ligase NEDD4 recruitment and ubiquitination of various activated GPCRs, including the β2 adrenergic receptor (β2AR) (Shenoy et al., 2008), and the μ-opioid (MOR) and V2 vasopressin receptors (V2R) (Groer et al., 2011), as a mechanism to segregate active receptors towards the degradative pathway following ubiquitin-specific binding to components of the ESCRT machinery and GPCR

sorting from endosomes to lysosomes (Mosesso et al., 2019), we have also investigated if a similar mechanism was in place for the GLP-1R which could potentially explain the differences in lysosomal targeting and sustained signal prolongation in β-arrestin 2-deleted beta cells, particularly as NEDD4 is one of the factors that we have recently identified as interacting with the GLP-1R in a mass-spectrometry analysis of the GLP-1R beta cell interactome. Unexpectedly, we have found the GLP-1R to be constitutively ubiquitinated, and then partially deubiquitinated following exendin-4 stimulation, a pattern that has also been recently observed for the closely related glucagon receptor (Kaur et al., 2020). In agreement, NEDD4 is also constitutively recruited to the receptor, and this recruitment gets reduced following exendin-4 stimulation. Importantly, there was a significant reduction in the overall level of GLP-1R ubiquitination and NEDD4 recruitment in cells with knocked-down β-arrestin 2, which, surprisingly, was present even under vehicle conditions. Constitutive GPCR ubiquitination often functions to control receptor trafficking through the biosynthetic pathway (Skieterska et al., 2017), but we did not find any differences in cell surface GLP-1R levels in control *versus* β-arrestin 2 knocked down beta cells. Additionally, constitutive ubiquitination of certain GPCRs promotes their basal internalisation and lysosomal degradation, whereas deubiquitination leads to recycling, switching the receptor's fate and enhancing cellular resensitisation (Alonso and Friedman, 2013; Skieterska et al., 2017). Our observations would fit with a complex mechanism of constitutive GLP-1R ubiquitination and exendin-4-mediated partial deubiquitination that is disrupted in the absence of β-arrestin 2, leading to divergent trafficking and signalling propensities.

In conclusion, we present here a comprehensive *in vivo*, *ex vivo* and *in vitro* assessment of the effects of knocking out β-arrestin 2 specifically from beta cells on pharmacological GLP-1R responses, which lead to reduced acute but enhanced sustained glucoregulation, that correlates with PDE4- and β-arrestin 1-dependent acute cAMP and downstream signalling defects but increased signal prolongation, as well as a trafficking phenotype consisting on the diversion of active GLP-1Rs from lysosomal compartments towards the TGN, which is accompanied by an overall reduction in GLP-1R ubiquitination and NEDD4 recruitment. Our study is the first to analyse in detail the consequences of the specific deletion of β-arrestin 2 from adult primary beta cells on GLP-1R behaviours. These data have important implications for the rational design of future GLP-1RAs with increased therapeutic windows.

Our study has several limitations, including the difficulty of adjusting experimental conditions to precisely translate *in vivo* acute and prolonged observations to corresponding *ex vivo* trafficking and signalling assessments. Additionally, our trafficking studies are performed with fluorescently

labelled exendin-4 and exendin-9 as a proxy for endogenous islet GLP-1R localisation, which is not exactly accurate. Better experiments could be performed in the future by using animals genetically modified to express SNAP- or HALO-tagged GLP-1Rs from the endogenous locus. Finally, mechanistic studies performed in INS-1 832/3 cells will require validation in primary islets and experiments will need to be designed to establish causation from correlative data such as the observed reduction in ubiquitination and its possible effects in modulating GLP-1R trafficking and sustained signalling.

Figure Legends

Figure 1. *In vivo* GLP-1R agonist responses in adult beta cell-specific β-arrestin 2 KO *vs* control mice on chow diet. IPGTTs (2 g/kg glucose i.p.) were performed concurrently with, or 6 h after, i.p. administration of agonists or vehicle (saline). (**a**) Schematic representation of the generation of Pdx1-Cre-ERT Barr2 fl/fl and control Barr2 fl/fl mice. (**b**) Diagram depicting the tamoxifen-induced adult beta cell-specific β-arrestin 2 (Barr2) KO mechanism using the Cre-lox system. (**c**) Relative gene expression of β-arrestin 2 (n = 4) and β-arrestin 1 (n = 6) in adult beta cell-specific β-arrestin 2 (β-Barr2) KO *vs* control mice. (**d**) Glucose curves and (**e**) corresponding ΔAUCs (6h-0h) for vehicle or exendin-4 (Ex-4) administration at 0.1, 1, and 10 nmol/kg in lean, male mice (n = 8-9 / genotype, age: 12-16 weeks). (**f**) Glucose curves and (**g**) corresponding ΔAUCs (6h-0h) for vehicle or Ex-4 administration at 0.1, 1, and 10 nmol/kg in lean, female mice (n = 9 / genotype, age: 12-16 weeks). (**h**) Glucose curves and (**i**) corresponding ΔAUCs (6h-0h) for vehicle, 1 nmol/kg Ex-4, or 1 nmol/kg Exendin-Phe1 (Ex-Phe1) administration in lean, female mice (n = 9 / genotype, age: 14-18 weeks). (**j**) Absolute and fold-change *vs* vehicle values for 10-min plasma insulin concentrations during IPGTTs (2 g/kg glucose i.p.) performed concurrently with, or 6 h after administration of vehicle or 1 nmol/kg Ex-4 in lean female mice (n = 7-9 / genotype, age: 12-16 weeks) with corresponding 6 h over acute fold changes included. Comparisons were made with unpaired t-tests, two-way ANOVA, or mixed-effects model with Sidak's *post hoc* tests. *p<0.05, **p<0.01, ****p<0.0001 *vs* control group. Data are presented as mean ± SEM.

Figure 2. *In vivo* GLP-1R agonist responses in adult beta cell-specific β-arrestin 2 KO *vs* control mice on high-fat, high-sucrose (HFHS) diet. (**a**) Weekly weights of male and female mice after HFHS diet initiation (n = 7-9 / genotype and sex). (**b**) Fasting and fed glycaemia of HSHF diet-fed male and female mice (n = 5-7 / genotype and sex, duration of HSHF diet: 10-16

weeks). (**c**) Glucose curves for vehicle or Ex-4 administration at 1 and 10 nmol/kg in HSHF diet-fed male mice (n = 7-9 / genotype, duration of HSHF diet: 8-12 weeks, initiated at 8 weeks of age). (**d**) Glucose curves for vehicle or Ex-4 administration at 1 and 10 nmol/kg in HSHF diet-fed female mice (n = 9 / genotype, duration of HSHF diet: 8-12 weeks, initiated at 8 weeks of age). (**e**) ΔAUCs (6h-0h) for male and female HFHS diet-fed mice from (c, d). (**f**) Normalised AUCs demonstrating the effect of Ex-4 *vs* vehicle ($AUC_{Exendin\text{-}4}/AUC_{vehicle}$) in HFHS diet-fed mice calculated from combined data presented in (c-e). (**g**) Glucose curves for vehicle, 10 nmol/kg semaglutide or 10 nmol/kg tirzepatide treatments; IPGTTs performed at 24 h or 72 h post-agonist i.p. injection in a mixed sex cohort (n = 8 / genotype, duration of HFHS diet: 8-12 weeks, initiated at 8 weeks of age). (**h**) Normalised AUCs demonstrating the agonist effect *vs* vehicle ($AUC_{agonist}/AUC_{vehicle}$) in HFHS diet-fed mice calculated from data presented in (g). (**i**) Absolute and fold-change *vs* vehicle values for 10-min plasma insulin concentrations during IPGTTs (2 g/kg glucose i.p.) performed concurrently with or 6 h after administration of vehicle or 1 nmol/kg Ex-4 in mixed male and female mice on HFHS diet (n = 7 / genotype, duration of HFHS diet: 10-16 weeks) with corresponding 6 h over acute fold changes included. Comparisons were made with unpaired t-tests, two-way ANOVA, or mixed-effects model with Sidak's *post hoc* tests. Fasting and fed glycaemia were compared within sex groups using one-way ANOVA with Sidak's *post hoc* test. *p<0.05, **p<0.01, ***p<0.001, ****p<0.0001 *vs* control group. Data are presented as mean ± SEM.

Figure 3. GLP-1R signalling alterations in adult beta cell-specific β-arrestin 2 KO *vs* control islets. (**a**) Schematic for the mouse generation and representative images of the CFP and YFP channels from a CAMPER islet. (**b**) Changes in FRET (YFP/CFP) over time in isolated beta cell-specific β-arrestin 2 (β-Barr2) KO *vs* control CAMPER islets in response to 100 nM Ex-4 followed by 100 μM IBMX; AUCs calculated for the Ex-4 treatment period (n = 5 / genotype). (**c**) Changes in FRET (YFP/CFP) over time in isolated β-Barr2 KO *vs* control CAMPER islets pre-treated with 1 nM Ex-4 for 16 h (overnight) in response to 1 nM GLP-1 stimulation followed by 100 μM IBMX; AUCs calculated for the indicated GLP-1 treatment period (n = 6 / genotype). (**d**, **e**) cAMP dose-response curves and corresponding Emax and logEC50 values in dispersed islets isolated from adult β-Barr2 KO and control mice on (d) chow diet (n= 5-6 / group) or (e) HFHS diet (n= 4-5 / group). (**f**) cAMP responses over time from cADDis-infected beta cell-specific Barr2 KO *vs* control islets in response to 100 nM Ex-4 followed by 100 μM IBMX + 10 μM forskolin (FSK); AUCs calculated for the Ex-4 treatment period (n = 4 / genotype). (**g**) cAMP responses over time from cADDis-infected β-Barr2 KO *vs* control islets pre-treated with 1 nM Ex-4 for 16 h (overnight) in

response to 1 nM GLP-1 stimulation followed by 100 μM IBMX + 10 μM FSK; AUCs calculated for the GLP-1 treatment period (n = 4 / genotype). (**h**) Changes in FRET (YFP/CFP) over time in isolated β-Barr2 KO *vs* control CAMPER islets in response to 100 nM Ex-4, 10 μM phosphodiesterase-4 inhibitor rolipram or a combination of the two; AUCs calculated for the indicated treatment period (n = 5 / genotype). (**i**) Representative images of the CFP and YFP channel and changes in FRET (YFP/CFP) over time in cells from dispersed β-Barr2 KO *vs* control CAMPER islets pre-treated with non-specific (ns) control or β-arrestin 1 (Barr1) siRNA for 72 h in response to 100 nM Ex-4 followed by 100 μM IBMX; AUCs calculated for the Ex-4 treatment period (n = 5-6 / genotype). Corresponding Barr1 over control siRNA-treated islet fold changes included for each condition. Comparisons were made with t-tests, two-way ANOVA, or mixed-effects model with Sidak's *post hoc* tests. *p<0.05, **p<0.01 *vs* control group. Data are presented as mean ± SEM.

Figure 4. Downstream effects of GLP-1R signalling alterations in adult beta cell-specific β-arrestin 2 KO *vs* control islets. (**a**) Calcium traces and corresponding AUCs and Emax for the indicated treatments in beta cell-specific β-arrestin 2 (β-Barr2) KO *vs* control islets isolated from animals on chow diet (n = 5 / genotype). (**b**) Calcium traces and corresponding AUCs and Emax for indicated treatments in β-Barr2 KO *vs* control islets isolated from animals on HFHS diet (n = 4 / genotype). (**c**, **d**) Representative cartesian connectivity maps (c) and percentage of connectivity (d) for β-Barr2 KO *vs* control GCaMP6f islets from HFHS diet donors implanted in the anterior chamber of the eye of WT acceptors on HFHS diet, which received 2 g/kg glucose i.p. with Ex-4 10 nmol/kg or saline (vehicle) (n = 6-8 islets / genotype). (**e**, **f**) Insulin secretion assays from control *vs* β-Barr2 KO islets treated with 100 nM Ex-4 or 100 nM GIP (fold over 11 mM glucose vehicle levels) for 1 h (acute) or 16 h (overnight) isolated from mice on (e) chow diet (n = 8 / genotype) or (f) HFHS diet (n = 6 / genotype). Corresponding overnight over acute fold changes included for each agonist. Comparisons between two experimental groups were made with t-tests or using one- or two-way ANOVA or mixed-effects model with Sidak's *post hoc* tests. *p<0.05, **p<0.01. Data are presented as mean ± SEM.

Figure 5. GLP-1R trafficking alterations in adult beta cell-specific β-arrestin 2 KO *vs* control islets. (**a**) Ex-4-TMR fluorescence at 1 h in beta cell-specific β-arrestin 2 (β-Barr2) KO *vs* control islets treated or not with acetic acid wash for 5 min before imaging for animals on chow (n = 6 / genotype) or HFHS diet (n = 4 / genotype). Normalisation of the fluorescence with *vs* without acid wash is used as a surrogate measure for GLP-1R internalisation (depicted for both diet

conditions). (**b**) Quantification of TMR fluorescence in β-Barr2 KO *vs* control islets pre-treated with vehicle or 100 nM Ex-4 for 1 h and then washed and treated with 100 nM Ex-4-TMR for 3 h for animals on chow (n = 6 / genotype) or HFHS diet (n = 4 / genotype). Normalisation of the fluorescence in Ex-4 over vehicle pre-treatment conditions is used as a surrogate measure for GLP-1R recycling (depicted for both diet conditions). (**c**) TMR fluorescence in β-Barr2 KO *vs* control islets pre-treated with vehicle or 100 nM Ex-4 for 1 h and then washed and treated with 100 nM Ex-4-TMR for 6 h in chow diet animals (n = 9 / genotype). Normalised fluorescence in Ex-4 over vehicle pre-treatment depicted as a surrogate measure for GLP-1R recycling. (**d**) Representative image of maximum intensity projections from confocal z-stacks, and quantification of TMR fluorescence in β-Barr2 KO *vs* control islets treated with 100 nM Ex-9-TMR for 30 min, as a measure for surface GLP-1R levels in animals on chow diet (n = 6 / genotype) or HFHS diet (n = 4 / genotype). (**e**) Representative images of maximum intensity projections from confocal z-stacks of β-Barr2 KO *vs* control islets labelled for Lamp1 (green) after treatment with 100 nM Ex-4-TMR (red) for 3 h. Manders' coefficient of co-localisation for Ex-4-TMR with Lamp1 signal is shown (n = 4 / genotype). (**f**) Representative images of maximum intensity projections from confocal z-stacks of β-Barr2 KO *vs* control islets labelled for TGN38 (green) after treatment with 100 nM Ex-4-TMR (red) for 3 h. Manders' coefficient of co-localisation for Ex-4-TMR with TGN38 signal is shown (n = 4 / genotype). (**g**) GLP-1R binding affinity to 100 nM Ex-4-TMR in β-Barr2 KO *vs* control islets pre-treated with metabolic inhibitors (n = 8 / genotype). Maximum value (YM), rate constant (k) and AUC from fitted curves are depicted for each genotype. Comparisons were made using t-tests, or two-way ANOVA with Sidak's *post hoc* tests. *$p<0.05$ *vs* control group. Data are presented as mean ± SEM.

Figure 6. Spatiotemporal signalling profiles of INS-1 832/3 β-arrestin 2 KD *vs* control beta cells. (**a**) Relative β-arrestin 2 gene expression in β-arrestin 2 (Barr2) KD *vs* control INS-1 832/3 cells (n = 3). (**b**) Ex-4 dose-response AUC curves for Nb37-SmBit and CAAX-LgBiT (plasma membrane) or Endofin-LgBiT (endosomal) signalling complementation assays (n = 5). (**c**) LogEC50 and Emax values calculated from (b). (**d**) Representative images of CFP and YFP channels from INS-1 832/3 cells transfected either with global (cytoplasmic) or TGN-targeted $^{T}Epac^{VV}$ cAMP biosensor constructs. (**e**) Changes in FRET (YFP/CFP) over time in INS-1 832/3 Barr2 KD *vs* control cells expressing global or TGN-targeted $^{T}Epac^{VV}$ cAMP biosensor constructs in response to 100 nM Ex-4 followed by 100 μM IBMX + 10 μM forskolin (n = 5). (**f**) AUCs calculated for the Ex-4 treatment period from (e). TGN-localised normalised to global cAMP AUCs are depicted for each cell type. (**g**) Representative blots for pERK1/2, total ERK1/2, pCREB, and

total CREB in Barr2 KD and control INS-1 832/3 cells at baseline (0 min) or after treatment with 100 nM Ex-4 for the indicated time-points. (**h**) Quantification of pERK1/2 over total ERK1/2 using densitometry analysis. Values normalised to baseline (fold *vs* vehicle) are also shown (n = 4). (**i**) Quantification of pCREB over total CREB using densitometry analysis. Values normalised to baseline (fold *vs* vehicle) are also shown (n = 3). Comparisons were made using t-tests, or two-way ANOVA with Sidak's *post hoc* tests. *p<0.05, **p<0.01, ***p<0.001, ****p<0.0001 *vs* control group. Data are presented as mean ± SEM.

Figure 7. Associated changes in GLP-1R trafficking and ubiquitination in INS-1 832/3 β-arrestin 2 KD *vs* control beta cells. (**a**) Endogenous surface GLP-1R receptor levels in untreated β-arrestin 2 (Barr2) KD *vs* control INS-1 832/3 cells quantified by labelling for 1 h with 1 μM Ex-9-TMR (n = 6). (**b**) Schematic representation of the principle of NanoBRET-based subcellular localisation assays. (**c**) Ex-4 dose-response AUC curves for SNAP-GLP-1R-NLuc and KRAS-Venus (plasma membrane), Rab5-Venus (early endosomes), and Rab11-Venus (recycling endosomes) NanoBRET assays (n = 5). (**d**) LogEC50 and Emax values calculated from (c). (**e**) AUC for NanoBRET responses to 100 nM Ex-4 using SNAP-GLP-1R-NLuc and Rab9-Venus (endosome-to-TGN) or Rab4-Venus (fast recycling endosomes). (**f**) Representative images of SNAP-GLP-1R-expressing Barr2 KD and control cells labelled with SNAP-Surface 647 (red) and treated with 100 nM Ex-4 or vehicle for 3 h and 1 μM LysoTracker Red DND-99 (green) for the last 5 min of the incubation period to label the lysosomes; Nuclei, DAPI (blue). (**g**) Manders' coefficient of co-localisation for SNAP-GLP-1R with LysoTracker Red DND-99 in INS-1 832/3 Barr2 KD *vs* control cells (n = 3). Ex-4 over vehicle fold values depicted as a surrogate measure of agonist-induced SNAP-GLP-1R degradation (n = 3). (**h**) Representative blots showing SNAP-GLP-1R and corresponding ubiquitination levels following SNAP-GLP-1R immunoprecipitation from INS-1 832/3 SNAP-GLP-1R Barr2 KD *vs* control cells under vehicle conditions of after stimulation with 100 nM Ex-4 for 10 min, with quantification of ubiquitin over SNAP levels for the different conditions shown (n = 8). (**i**) Quantification of SNAP-GLP-1R deubiquitination in response to 10 min of 100 nM Ex-4 exposure in INS-1 832/3 SNAP-GLP-1R control and Barr2 KD cells. Data from (h) normalised to vehicle conditions for each cell type. (**j**) Representative blots showing SNAP-GLP-1R and HA-NEDD4 levels following SNAP-GLP-1R immunoprecipitation from INS-1 832/3 SNAP-GLP-1R Barr2 KD *vs* control cells under vehicle conditions of after stimulation with 100 nM Ex-4 for 10 min, with quantification of HA over SNAP levels for the different conditions shown (n = 4). (**k**) Quantification of loss of HA-NEDD4 - SNAP-GLP-1R interaction in response to 10 min of 100 nM Ex-4 exposure in INS-1 832/3 SNAP-GLP-1R Barr2

KD and control cells. Data from (j) normalised to vehicle conditions for each cell type. Comparisons were performed using t-tests, ratio-t-tests, or one- or two-way ANOVA with Sidak's *post hoc* tests. *p<0.05, **p<0.01, ***p<0.001. Data are presented as mean ± SEM.

Extended Data Figure Legends

Extended Data Figure 1. GLP-1R agonist responses in adult beta cell-specific β-arrestin 2 KO *vs* control mice – extra data. (**a**, **b**) Weight (a), and fasting and fed glycaemia (b) of lean adult beta cell-specific β-arrestin 2 (β-Barr2) KO *vs* control male and female mice (n = 6-9 / genotype and sex, age: 20-24 weeks). (**c**) Representative EM images depicting islet ultrastructure and quantification of insulin granule densities in islets isolated from lean adult β-Barr2 KO *vs* control mice on chow diet (n = 5). (**d** - **k**) IPGTTs (2 g/kg glucose i.p.) performed concurrently with or 6 h after i.p. administration of agonists or vehicle (saline). (**d**) Glucose curves and (**e**) corresponding ΔAUCs (6h-0h) for vehicle or D-Ala^2-GIP administration at 10 and 40 nmol/kg in lean male mice (n = 8 / genotype, age: 18-26 weeks). (**f**) Glucose curves and (**g**) corresponding ΔAUCs (6h-0h) for vehicle or D-Ala^2-GIP administration at 10 and 40 nmol/kg in lean female mice (n = 8-9 / genotype, age: 18-26 weeks). (**h**) Glucose curves and (**i**) corresponding ΔAUCs (6h-0h) for vehicle or Ex-4 administration at 0.1, 1, and 10 nmol/kg in tamoxifen-inducible whole-body (R26-Cre-ERT) Barr2 KO and control lean males (n = 8 / genotype, age: 12-16 weeks). (**j**) Glucose curves and (**k**) corresponding ΔAUCs (6h-0h) for vehicle or Ex-4 administration at 0.1, 1, and 10 nmol/kg in tamoxifen-inducible whole-body (R26-Cre-ERT) Barr2 KO and control lean females (n = 8 / genotype, age: 12-16 weeks). Comparisons were performed using unpaired t-tests or one- or two-way ANOVA or mixed-effects model with Sidak's *post hoc* tests. Data are presented as mean ± SEM.

Extended Data Figure 2. Alpha and beta cell mass and gene expression patterns from adult beta cell-specific β-arrestin 2 KO *vs* control islets. (**a**) Representative images of pancreatic sections from adult beta cell-specific β-arrestin 2 (β-Barr2) KO *vs* control mice on HFHS diet depicting islets with nuclei stained with DAPI (blue) and co-stained for insulin (green) and glucagon (red). (**b**) Quantifications of beta and alpha cell mass, alpha/beta cell mass ratio and average islet sizes in adult β-Barr2 KO *vs* control mice on HFHS diet (n = 5-6 / group). (**c**, **d**) Relative gene expression of selected beta cell-enriched and -disallowed genes in control *vs* adult β-Barr2 KO mice on (c) chow diet (n = 6) or (d) HFHS diet (n = 4). Comparisons were made using

unpaired t-tests or two-way ANOVA with Sidak's *post hoc* tests. *p<0.05, **p<0.01, ***p<0.001 *vs* control group. Data are presented as mean ± SEM.

Extended Data Figure 3. Extra connectivity data from adult beta cell-specific β-arrestin 2 KO *vs* control islets implanted in the anterior chamber of the eye. (**a**, **b**) Percentage of islets within each wave activity index category for (a) chow and (b) HFHS diet animals (n = 6-13 islets / condition). (**c**, **d**) Calcium wave characteristics: amplitude, wavelength, and full width at half maximum (FWHM) for beta cell-specific β-arrestin 2 (β-Barr2) KO *vs* control GCaMP6f islets from donors implanted in the anterior chamber of the eye from (c) chow and (d) HFSH diet experiments (n = 0-13 islets / condition). (**e**) Percentage of connectivity for β-Barr2 KO *vs* control GCaMP6f islets from chow diet animals implanted in the anterior chamber of the eye of chow diet-fed WT animals, which received Ex-4 10 nmol/kg or saline (vehicle) i.p. (n = 2-11 islets / condition). Comparisons were made with two-way ANOVA with Sidak's *post hoc* tests. *p<0.05, **p<0.01 *vs* control group. Data are presented as mean ± SEM.

Extended Data Figure 4. *In vivo* agonist uptake data from adult beta cell-specific β-arrestin 2 KO *vs* control islets. (**a**) Representative images from optical projection tomography data from pancreata extracted from whole-body β-arrestin 2 (Barr2) KO and control animals injected i.p. with 100 nmol/kg Ex-4-VT750 1 h or 6 h post-injection. (**b**) Mean Ex-4-VT750 islet fluorescence in whole pancreata extracted from Barr2 KO and control animals injected i.p. with 100 nmol/kg Ex-4-VT750 1 h or 6 h prior to sacrifice (n = 6 / genotype). Comparisons were made using t-tests, or two-way ANOVA with Sidak's *post hoc* tests; *p<0.05. Data are presented as mean ± SEM.

Extended Data Figure 5. β-arrestin 2 recruitment dynamics in INS-1 832/3 SNAP-GLP-1R cells. (**a**) Time-lapse spinning disk imaging of SNAP-GLP-1R (red) and β-arrestin 2-GFP (green) dynamic profiles in INS-1 832/3 SNAP-GLP-1R cells in response to 100 nM Ex-4. Selected time frames are depicted for the green, red and merged channels. **(b**) High magnification image for the 5-min stimulation time-point from (a). Areas of SNAP-GLP-1R - β-arrestin 2-GFP co-localisation are indicated with white arrows.

Extended Data Figure 6. GIPR responses in β-arrestin 2 KD *vs* control INS-1 832/3 cell lines. (**a**) D-Ala^{2}GIP dose-response AUC curves for Nb37-SmBiT and CAAX-LgBiT (plasma membrane) or Endofin-LgBiT (endosomal) signal complementation assays (n = 5). (**b**) LogEC50 and Emax values calculated from (a). Data are presented as mean ± SEM.

Acknowledgements

This work was supported by MRC grant number MR/R010676/1 to A.T., B.J. and G.A.R., and by UKRI COVID-19 Grant Extension Allocation (coA) to A.T. A.T. also acknowledges support from the EFSD, Diabetes UK, Eli Lilly, the Commonwealth and the Integrated Biological Imaging Network (IBIN). S.B. was supported by an Early Career Grant from the Society for Endocrinology. The authors thank Mr Stephen Rothery from the National Heart and Lung Institute (NHLI) Facility for Imaging by Light Microscopy (FILM), Imperial College London, for technical assistance and help with data analysis, Dr Pauline Chabosseau for providing a macro for beta and alpha cell mass quantification in Image J and Dr Sebastien Goudreau from ImmuPharma Group, France, for the synthesis of exendin-4-VT750.

References

Abdullah, N., M. Beg, D. Soares, J.S. Dittman, and T.E. McGraw. 2016. Downregulation of a GPCR by beta-Arrestin2-Mediated Switch from an Endosomal to a TGN Recycling Pathway. *Cell Rep*. 17:2966-2978.

Alonso, V., and P.A. Friedman. 2013. Minireview: ubiquitination-regulated G protein-coupled receptor signaling and trafficking. *Mol Endocrinol*. 27:558-572.

Baillie, G.S., A. Sood, I. McPhee, I. Gall, S.J. Perry, R.J. Lefkowitz, and M.D. Houslay. 2003. beta-Arrestin-mediated PDE4 cAMP phosphodiesterase recruitment regulates beta-adrenoceptor switching from Gs to Gi. *Proc Natl Acad Sci U S A*. 100:940-945.

Benner, C., T. van der Meulen, E. Caceres, K. Tigyi, C.J. Donaldson, and M.O. Huising. 2014. The transcriptional landscape of mouse beta cells compared to human beta cells reveals notable species differences in long non-coding RNA and protein-coding gene expression. *BMC Genomics*. 15:620.

Bettge, K., M. Kahle, M.S. Abd El Aziz, J.J. Meier, and M.A. Nauck. 2017. Occurrence of nausea, vomiting and diarrhoea reported as adverse events in clinical trials studying glucagon-like peptide-1 receptor agonists: A systematic analysis of published clinical trials. *Diabetes Obes Metab*. 19:336-347.

Blodgett, D.M., A. Nowosielska, S. Afik, S. Pechhold, A.J. Cura, N.J. Kennedy, S. Kim, A. Kucukural, R.J. Davis, S.C. Kent, D.L. Greiner, M.G. Garber, D.M. Harlan, and P. diIorio. 2015. Novel Observations From Next-Generation RNA Sequencing of Highly Purified Human Adult and Fetal Islet Cell Subsets. *Diabetes*. 64:3172-3181.

Buenaventura, T., S. Bitsi, W.E. Laughlin, T. Burgoyne, Z. Lyu, A.I. Oqua, H. Norman, E.R. McGlone, A.S. Klymchenko, I.R. Corrêa, A. Walker, A. Inoue, A. Hanyaloglu, J. Grimes, Z. Koszegi, D. Calebiro, G.A. Rutter, S.R. Bloom, B. Jones, and A. Tomas. 2019. Agonist-induced membrane nanodomain clustering drives GLP-1 receptor responses in pancreatic beta cells. *PLoS Biol*. 17:e3000097.

Buenaventura, T., N. Kanda, P.C. Douzenis, B. Jones, S.R. Bloom, P. Chabosseau, I.R. Correa, Jr., D. Bosco, L. Piemonti, P. Marchetti, P.R. Johnson, A.M.J. Shapiro, G.A. Rutter, and A. Tomas. 2018. A Targeted RNAi Screen Identifies Endocytic Trafficking Factors That Control GLP-1 Receptor Signaling in Pancreatic beta-Cells. *Diabetes*. 67:385-399.

Chen, T.W., T.J. Wardill, Y. Sun, S.R. Pulver, S.L. Renninger, A. Baohan, E.R. Schreiter, R.A. Kerr, M.B. Orger, V. Jayaraman, L.L. Looger, K. Svoboda, and D.S. Kim. 2013. Ultrasensitive fluorescent proteins for imaging neuronal activity. *Nature*. 499:295-300.

Dores, M.R., and J. Trejo. 2019. Endo-lysosomal sorting of G-protein-coupled receptors by ubiquitin: Diverse pathways for G-protein-coupled receptor destruction and beyond. *Traffic*. 20:101-109.

Ertürk, A., K. Becker, N. Jährling, C.P. Mauch, C.D. Hojer, J.G. Egen, F. Hellal, F. Bradke, M. Sheng, and H.-U. Dodt. 2012. Three-dimensional imaging of solvent-cleared organs using 3DISCO. *Nature Protocols*. 7:1983-1995.

Faerch, K., S.S. Torekov, D. Vistisen, N.B. Johansen, D.R. Witte, A. Jonsson, O. Pedersen, T. Hansen, T. Lauritzen, A. Sandbaek, J.J. Holst, and M.E. Jorgensen. 2015. GLP-1 Response to Oral Glucose Is Reduced in Prediabetes, Screen-Detected Type 2 Diabetes, and Obesity and Influenced by Sex: The ADDITION-PRO Study. *Diabetes*. 64:2513-2525.

Fang, Z., S. Chen, Y. Manchanda, S. Bitsi, P. Pickford, A. David, M.M. Shchepinova, I.R. Correa, Jr., D.J. Hodson, J. Broichhagen, E.W. Tate, F. Reimann, V. Salem, G.A. Rutter, T. Tan, S.R. Bloom, A. Tomas, and B. Jones. 2020. Ligand-Specific Factors Influencing GLP-1 Receptor Post-Endocytic Trafficking and Degradation in Pancreatic Beta Cells. *Int J Mol Sci*. 21.

Ferguson, S.S., W.E. Downey, 3rd, A.M. Colapietro, L.S. Barak, L. Ménard, and M.G. Caron. 1996. Role of beta-arrestin in mediating agonist-promoted G protein-coupled receptor internalization. *Science*. 271:363-366.

Frias, J.P., M.J. Davies, J. Rosenstock, F.C. Perez Manghi, L. Fernandez Lando, B.K. Bergman, B. Liu, X. Cui, K. Brown, and S.-. Investigators. 2021. Tirzepatide versus Semaglutide Once Weekly in Patients with Type 2 Diabetes. *N Engl J Med*. 385:503-515.

Fu, A., A.C. Ng, C. Depatie, N. Wijesekara, Y. He, G.S. Wang, N. Bardeesy, F.W. Scott, R.M. Touyz, M.B. Wheeler, and R.A. Screaton. 2009. Loss of Lkb1 in adult beta cells increases beta cell mass and enhances glucose tolerance in mice. *Cell Metab*. 10:285-295.

Godbole, A., S. Lyga, M.J. Lohse, and D. Calebiro. 2017. Internalized TSH receptors en route to the TGN induce local Gs-protein signaling and gene transcription. *Nat Commun*. 8:443.

Groer, C.E., C.L. Schmid, A.M. Jaeger, and L.M. Bohn. 2011. Agonist-directed interactions with specific beta-arrestins determine mu-opioid receptor trafficking, ubiquitination, and dephosphorylation. *J Biol Chem*. 286:31731-31741.

Hammad, S., A. Othman, C. Meyer, A. Telfah, J. Lambert, B. Dewidar, J. Werle, Z.C. Nwosu, A. Mahli, C. Dormann, Y. Gao, K. Gould, M. Han, X. Yuan, M. Gogiashvili, R. Hergenröder, C. Hellerbrand, M. Thomas, M.P. Ebert, S. Amasheh, J.G. Hengstler, and S. Dooley. 2018. Confounding influence of tamoxifen in mouse models of Cre recombinase-induced gene activity or modulation. *Arch Toxicol*. 92:2549-2561.

Hodson, D.J., R.K. Mitchell, E.A. Bellomo, G. Sun, L. Vinet, P. Meda, D. Li, W.H. Li, M. Bugliani, P. Marchetti, D. Bosco, L. Piemonti, P. Johnson, S.J. Hughes, and G.A. Rutter. 2013. Lipotoxicity disrupts incretin-regulated human beta cell connectivity. *J Clin Invest*. 123:4182-4194.

Irannejad, R., J.C. Tomshine, J.R. Tomshine, M. Chevalier, J.P. Mahoney, J. Steyaert, S.G. Rasmussen, R.K. Sunahara, H. El-Samad, B. Huang, and M. von Zastrow. 2013. Conformational biosensors reveal GPCR signalling from endosomes. *Nature*. 495:534-538.

Johnston, N.R., R.K. Mitchell, E. Haythorne, M.P. Pessoa, F. Semplici, J. Ferrer, L. Piemonti, P. Marchetti, M. Bugliani, D. Bosco, E. Berishvili, P. Duncanson, M. Watkinson, J. Broichhagen, D. Trauner, G.A. Rutter, and D.J. Hodson. 2016. Beta Cell Hubs Dictate Pancreatic Islet Responses to Glucose. *Cell Metab*. 24:389-401.

Jones, B. 2021. The therapeutic potential of GLP-1 receptor biased agonism. *Br J Pharmacol*.

Jones, B., T. Buenaventura, N. Kanda, P. Chabosseau, B.M. Owen, R. Scott, R. Goldin, N. Angkathunyakul, I.R. Corrêa, D. Bosco, P.R. Johnson, L. Piemonti, P. Marchetti, A.M.J. Shapiro, B.J. Cochran, A.C. Hanyaloglu, A. Inoue, T. Tan, G.A. Rutter, A. Tomas, and S.R. Bloom. 2018. Targeting GLP-1 receptor trafficking to improve agonist efficacy. *Nat Commun*. 9:1602.

Jones, B., E.R. McGlone, Z. Fang, P. Pickford, I.R. Correa, Jr., A. Oishi, R. Jockers, A. Inoue, S. Kumar, F. Gorlitz, C. Dunsby, P.M.W. French, G.A. Rutter, T. Tan, A. Tomas, and S.R. Bloom. 2021. Genetic and biased agonist-mediated reductions in beta-arrestin recruitment prolong cAMP signaling at glucagon family receptors. *J Biol Chem*. 296:100133.

Kaur, S., Y. Chen, and S.K. Shenoy. 2020. Agonist-activated glucagon receptors are deubiquitinated at early endosomes by two distinct deubiquitinases to facilitate Rab4a-dependent recycling. *J Biol Chem*. 295:16630-16642.

Kilanowska, A., and A. Ziółkowska. 2020. Role of Phosphodiesterase in the Biology and Pathology of Diabetes. *Int J Mol Sci*. 21.

Klarenbeek, J.B., J. Goedhart, M.A. Hink, T.W.J. Gadella, and K. Jalink. 2011. A mTurquoise-Based cAMP Sensor for Both FLIM and Ratiometric Read-Out Has Improved Dynamic Range. *PLOS ONE*. 6:e19170.

Kühn, H., and U. Wilden. 1987. Deactivation of photoactivated rhodopsin by rhodopsin-kinase and arrestin. *J Recept Res*. 7:283-298.

Laporte, S.A., R.H. Oakley, J.A. Holt, L.S. Barak, and M.G. Caron. 2000. The Interaction of β-Arrestin with the AP-2 Adaptor Is Required for the Clustering of β₂-Adrenergic Receptor into Clathrin-coated Pits *. *Journal of Biological Chemistry*. 275:23120-23126.

Li, X., C. Clappier, I. Kleiter, and R. Heuchel. 2019. Tamoxifen affects chronic pancreatitis-related fibrogenesis in an experimental mouse model: an effect beyond Cre recombination. *FEBS Open Bio*. 9:1756-1768.

Livak, K.J., and T.D. Schmittgen. 2001. Analysis of relative gene expression data using real-time quantitative PCR and the 2(-Delta Delta C(T)) Method. *Methods*. 25:402-408.

Lohse, M.J., J.L. Benovic, J. Codina, M.G. Caron, and R.J. Lefkowitz. 1990. beta-Arrestin: a protein that regulates beta-adrenergic receptor function. *Science*. 248:1547-1550.

Lohse, M.J., and C. Hoffmann. 2014. Arrestin interactions with G protein-coupled receptors. *Handb Exp Pharmacol*. 219:15-56.

Lucey, M., T. Ashik, A. Marzook, Y. Wang, J. Goulding, A. Oishi, J. Broichhagen, D.J. Hodson, J. Minnion, Y. Elani, R. Jockers, S.J. Briddon, S.R. Bloom, A. Tomas, and B. Jones. 2021. Acylation of the Incretin Peptide Exendin-4 Directly Impacts Glucagon-Like Peptide-1 Receptor Signaling and Trafficking. *Mol Pharmacol*. 100:319-334.

Luttrell, L.M., S.S. Ferguson, Y. Daaka, W.E. Miller, S. Maudsley, G.J. Della Rocca, F. Lin, H. Kawakatsu, K. Owada, D.K. Luttrell, M.G. Caron, and R.J. Lefkowitz. 1999. Beta-arrestin-dependent formation of beta2 adrenergic receptor-Src protein kinase complexes. *Science*. 283:655-661.

Luttrell, L.M., F.L. Roudabush, E.W. Choy, W.E. Miller, M.E. Field, K.L. Pierce, and R.J. Lefkowitz. 2001. Activation and targeting of extracellular signal-regulated kinases by beta-arrestin scaffolds. *Proc Natl Acad Sci U S A*. 98:2449-2454.

Martinez-Sanchez, A., M.S. Nguyen-Tu, and G.A. Rutter. 2015. DICER Inactivation Identifies Pancreatic β-Cell "Disallowed" Genes Targeted by MicroRNAs. *Mol Endocrinol*. 29:1067-1079.

Marzook, A., A. Tomas, and B. Jones. 2021. The Interplay of Glucagon-Like Peptide-1 Receptor Trafficking and Signalling in Pancreatic Beta Cells. *Front Endocrinol (Lausanne)*. 12:678055.

McGlone, E.R., Y. Manchanda, B. Jones, P. Pickford, A. Inoue, D. Carling, S.R. Bloom, T. Tan, and A. Tomas. 2021. Receptor Activity-Modifying Protein 2 (RAMP2) alters glucagon

receptor trafficking in hepatocytes with functional effects on receptor signalling. *Mol Metab*. 53:101296.

Miguel-Escalada, I., S. Bonàs-Guarch, I. Cebola, J. Ponsa-Cobas, J. Mendieta-Esteban, G. Atla, B.M. Javierre, D.M.Y. Rolando, I. Farabella, C.C. Morgan, J. García-Hurtado, A. Beucher, I. Morán, L. Pasquali, M. Ramos-Rodríguez, E.V.R. Appel, A. Linneberg, A.P. Gjesing, D.R. Witte, O. Pedersen, N. Grarup, P. Ravassard, D. Torrents, J.M. Mercader, L. Piemonti, T. Berney, E.J.P. de Koning, J. Kerr-Conte, F. Pattou, I.O. Fedko, L. Groop, I. Prokopenko, T. Hansen, M.A. Marti-Renom, P. Fraser, and J. Ferrer. 2019. Human pancreatic islet three-dimensional chromatin architecture provides insights into the genetics of type 2 diabetes. *Nature Genetics*. 51:1137-1148.

Mosesso, N., M.K. Nagel, and E. Isono. 2019. Ubiquitin recognition in endocytic trafficking - with or without ESCRT-0. *J Cell Sci*. 132.

Muntean, B.S., S. Zucca, C.M. MacMullen, M.T. Dao, C. Johnston, H. Iwamoto, R.D. Blakely, R.L. Davis, and K.A. Martemyanov. 2018. Interrogating the Spatiotemporal Landscape of Neuromodulatory GPCR Signaling by Real-Time Imaging of cAMP in Intact Neurons and Circuits. *Cell Rep*. 24:1081-1084.

Nauck, M.A., D.R. Quast, J. Wefers, and J.J. Meier. 2021. GLP-1 receptor agonists in the treatment of type 2 diabetes - state-of-the-art. *Mol Metab*. 46:101102.

Parruti, G., F. Peracchia, M. Sallese, G. Ambrosini, M. Masini, D. Rotilio, and A. De Blasi. 1993. Molecular analysis of human beta-arrestin-1: cloning, tissue distribution, and regulation of expression. Identification of two isoforms generated by alternative splicing. *J Biol Chem*. 268:9753-9761.

Perry, S.J., G.S. Baillie, T.A. Kohout, I. McPhee, M.M. Magiera, K.L. Ang, W.E. Miller, A.J. McLean, M. Conti, M.D. Houslay, and R.J. Lefkowitz. 2002. Targeting of cyclic AMP degradation to beta 2-adrenergic receptors by beta-arrestins. *Science*. 298:834-836.

Pickford, P., M. Lucey, Z. Fang, S. Bitsi, J.B. de la Serna, J. Broichhagen, D.J. Hodson, J. Minnion, G.A. Rutter, S.R. Bloom, A. Tomas, and B. Jones. 2020. Signalling, trafficking and glucoregulatory properties of glucagon-like peptide-1 receptor agonists exendin-4 and lixisenatide. *Br J Pharmacol*. 177:3905-3923.

Pullen, T.J., A.M. Khan, G. Barton, S.A. Butcher, G. Sun, and G.A. Rutter. 2010. Identification of genes selectively disallowed in the pancreatic islet. *Islets*. 2:89-95.

Pyne, N.J., and B.L. Furman. 2003. Cyclic nucleotide phosphodiesterases in pancreatic islets. *Diabetologia*. 46:1179-1189.

Quoyer, J., C. Longuet, C. Broca, N. Linck, S. Costes, E. Varin, J. Bockaert, G. Bertrand, and S. Dalle. 2010. GLP-1 mediates antiapoptotic effect by phosphorylating Bad through a beta-arrestin 1-mediated ERK1/2 activation in pancreatic beta-cells. *J Biol Chem*. 285:1989-2002.

Ravier, M.A., M. Leduc, J. Richard, N. Linck, A. Varrault, N. Pirot, M.M. Roussel, J. Bockaert, S. Dalle, and G. Bertrand. 2014. beta-Arrestin2 plays a key role in the modulation of the pancreatic beta cell mass in mice. *Diabetologia*. 57:532-541.

Saleh, N., G. Saladino, F.L. Gervasio, and T. Clark. 2017. Investigating allosteric effects on the functional dynamics of beta2-adrenergic ternary complexes with enhanced-sampling simulations. *Chem Sci*. 8:4019-4026.

Salem, V., L.D. Silva, K. Suba, E. Georgiadou, S. Neda Mousavy Gharavy, N. Akhtar, A. Martin-Alonso, D.C.A. Gaboriau, S.M. Rothery, T. Stylianides, G. Carrat, T.J. Pullen, S.P. Singh, D.J. Hodson, I. Leclerc, A.M.J. Shapiro, P. Marchetti, L.J.B. Briant, W. Distaso, N. Ninov, and G.A. Rutter. 2019. Leader beta-cells coordinate Ca(2+) dynamics across pancreatic islets in vivo. *Nat Metab*. 1:615-629.

Sanni, S.J., J.T. Hansen, M.M. Bonde, T. Speerschneider, G.L. Christensen, S. Munk, S. Gammeltoft, and J.L. Hansen. 2010. beta-Arrestin 1 and 2 stabilize the angiotensin II type I receptor in distinct high-affinity conformations. *Br J Pharmacol*. 161:150-161.

Shenoy, S.K., K. Xiao, V. Venkataramanan, P.M. Snyder, N.J. Freedman, and A.M. Weissman. 2008. Nedd4 mediates agonist-dependent ubiquitination, lysosomal targeting, and degradation of the beta2-adrenergic receptor. *J Biol Chem*. 283:22166-22176.

Skieterska, K., P. Rondou, and K. Van Craenenbroeck. 2017. Regulation of G Protein-Coupled Receptors by Ubiquitination. *Int J Mol Sci*. 18.

Sonoda, N., T. Imamura, T. Yoshizaki, J.L. Babendure, J.C. Lu, and J.M. Olefsky. 2008. Beta-Arrestin-1 mediates glucagon-like peptide-1 signaling to insulin secretion in cultured pancreatic beta cells. *Proc Natl Acad Sci U S A*. 105:6614-6619.

Srivastava, A., B. Gupta, C. Gupta, and A.K. Shukla. 2015. Emerging Functional Divergence of β-Arrestin Isoforms in GPCR Function. *Trends Endocrinol Metab*. 26:628-642.

Tewson, P.H., S. Martinka, N.C. Shaner, T.E. Hughes, and A.M. Quinn. 2016. New DAG and cAMP Sensors Optimized for Live-Cell Assays in Automated Laboratories. *J Biomol Screen*. 21:298-305.

Thompson, A., and V. Kanamarlapudi. 2015. Agonist-induced internalisation of the glucagon-like peptide-1 receptor is mediated by the Gαq pathway. *Biochem Pharmacol*. 93:72-84.

Tramunt, B., S. Smati, N. Grandgeorge, F. Lenfant, J.F. Arnal, A. Montagner, and P. Gourdy. 2020. Sex differences in metabolic regulation and diabetes susceptibility. *Diabetologia*. 63:453-461.

van Gastel, J., J.O. Hendrickx, H. Leysen, P. Santos-Otte, L.M. Luttrell, B. Martin, and S. Maudsley. 2018. β-Arrestin Based Receptor Signaling Paradigms: Potential Therapeutic Targets for Complex Age-Related Disorders. *Frontiers in Pharmacology*. 9:1369.

Wang, Z.W., X. Hu, M. Ye, M. Lin, M. Chu, and X. Shen. 2020. NEDD4 E3 ligase: Functions and mechanism in human cancer. *Semin Cancer Biol*. 67:92-101.

Wess, J. 2022. The Two beta-Arrestins Regulate Distinct Metabolic Processes: Studies with Novel Mutant Mouse Models. *Int J Mol Sci*. 23.

Willard, F.S., J.D. Douros, M.B. Gabe, A.D. Showalter, D.B. Wainscott, T.M. Suter, M.E. Capozzi, W.J. van der Velden, C. Stutsman, G.R. Cardona, S. Urva, P.J. Emmerson, J.J. Holst, D.A. D'Alessio, M.P. Coghlan, M.M. Rosenkilde, J.E. Campbell, and K.W. Sloop. 2020. Tirzepatide is an imbalanced and biased dual GIP and GLP-1 receptor agonist. *JCI Insight*. 5.

Willis, M.J., and G.S. Baillie. 2014. Arrestin-dependent localization of phosphodiesterases. *Handb Exp Pharmacol*. 219:293-307.

Zhang, H., E. Sturchler, J. Zhu, A. Nieto, P.A. Cistrone, J. Xie, L. He, K. Yea, T. Jones, R. Turn, P.S. Di Stefano, P.R. Griffin, P.E. Dawson, P.H. McDonald, and R.A. Lerner. 2015. Autocrine selection of a GLP-1R G-protein biased agonist with potent antidiabetic effects. *Nat Commun*. 6:8918.

Zhu, J., E. Mix, and B. Winblad. 2001. The antidepressant and antiinflammatory effects of rolipram in the central nervous system. *CNS Drug Rev*. 7:387-398.

Zhu, L., J. Almaca, P.K. Dadi, H. Hong, W. Sakamoto, M. Rossi, R.J. Lee, N.C. Vierra, H. Lu, Y. Cui, S.M. McMillin, N.A. Perry, V.V. Gurevich, A. Lee, B. Kuo, R.D. Leapman, F.M. Matschinsky, N.M. Doliba, N.M. Urs, M.G. Caron, D.A. Jacobson, A. Caicedo, and J. Wess. 2017. beta-arrestin-2 is an essential regulator of pancreatic beta-cell function under physiological and pathophysiological conditions. *Nat Commun*. 8:14295.

Figure 1

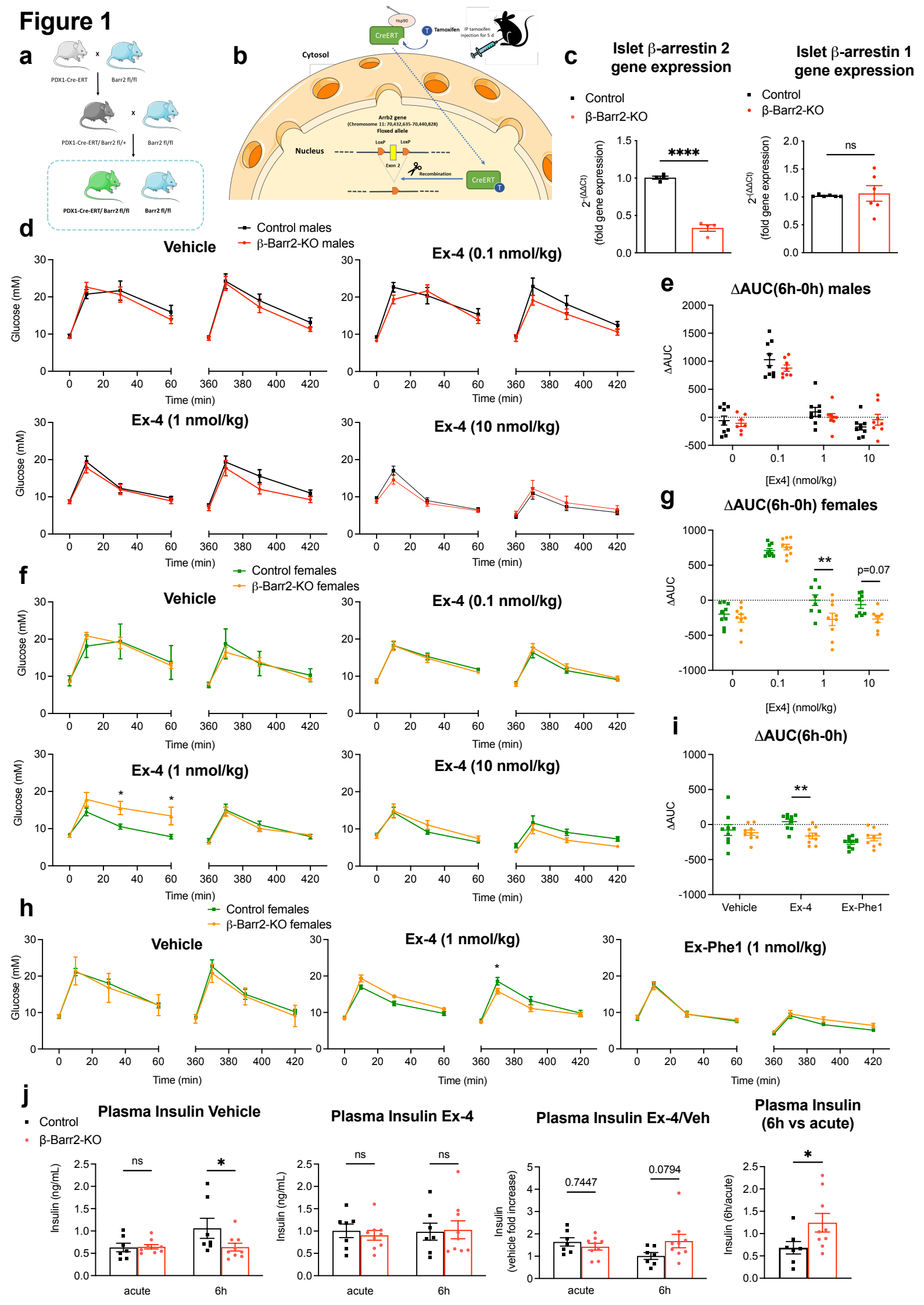
a
PDX1-Cre-ERT
Barr2 fl/fl
PDX1-Cre-ERT/ Barr2 fl/+
Barr2 fl/fl
PDX1-Cre-ERT/ Barr2 fl/fl
Barr2 fl/fl
b
Cytosol
Hsp90
CreERT
Tamoxifen
IP tamoxifen injection for 5 d
Arrb2 gene
(Chromosome 11: 70,432,635-70,440,828)
Floxed allele
Nucleus
LoxP
LoxP
Exon 2
Recombination
CreERT
c
Islet β-arrestin 2 gene expression
Control
β-Barr2-KO
****
2^-(ΔΔCt) (fold gene expression)
Islet β-arrestin 1 gene expression
Control
β-Barr2-KO
ns
2^-(ΔΔCt) (fold gene expression)
d
Control males
β-Barr2-KO males
Vehicle
Ex-4 (0.1 nmol/kg)
Ex-4 (1 nmol/kg)
Ex-4 (10 nmol/kg)
Glucose (mM)
Time (min)
e
ΔAUC(6h-0h) males
ΔAUC
[Ex4] (nmol/kg)
g
ΔAUC(6h-0h) females
**
p=0.07
ΔAUC
[Ex4] (nmol/kg)
f
Control females
β-Barr2-KO females
Vehicle
Ex-4 (0.1 nmol/kg)
Ex-4 (1 nmol/kg)
Ex-4 (10 nmol/kg)
Glucose (mM)
Time (min)
i
ΔAUC(6h-0h)
**
ΔAUC
Vehicle
Ex-4
Ex-Phe1
h
Control females
β-Barr2-KO females
Vehicle
Ex-4 (1 nmol/kg)
Ex-Phe1 (1 nmol/kg)
Glucose (mM)
Time (min)
j
Control
β-Barr2-KO
Plasma Insulin Vehicle
Plasma Insulin Ex-4
Plasma Insulin Ex-4/Veh
Plasma Insulin (6h vs acute)
Insulin (ng/mL)
ns
*
ns
ns
Insulin (vehicle fold increase)
0.7447
0.0794
Insulin (6h/acute)
*
acute
6h

Figure 2

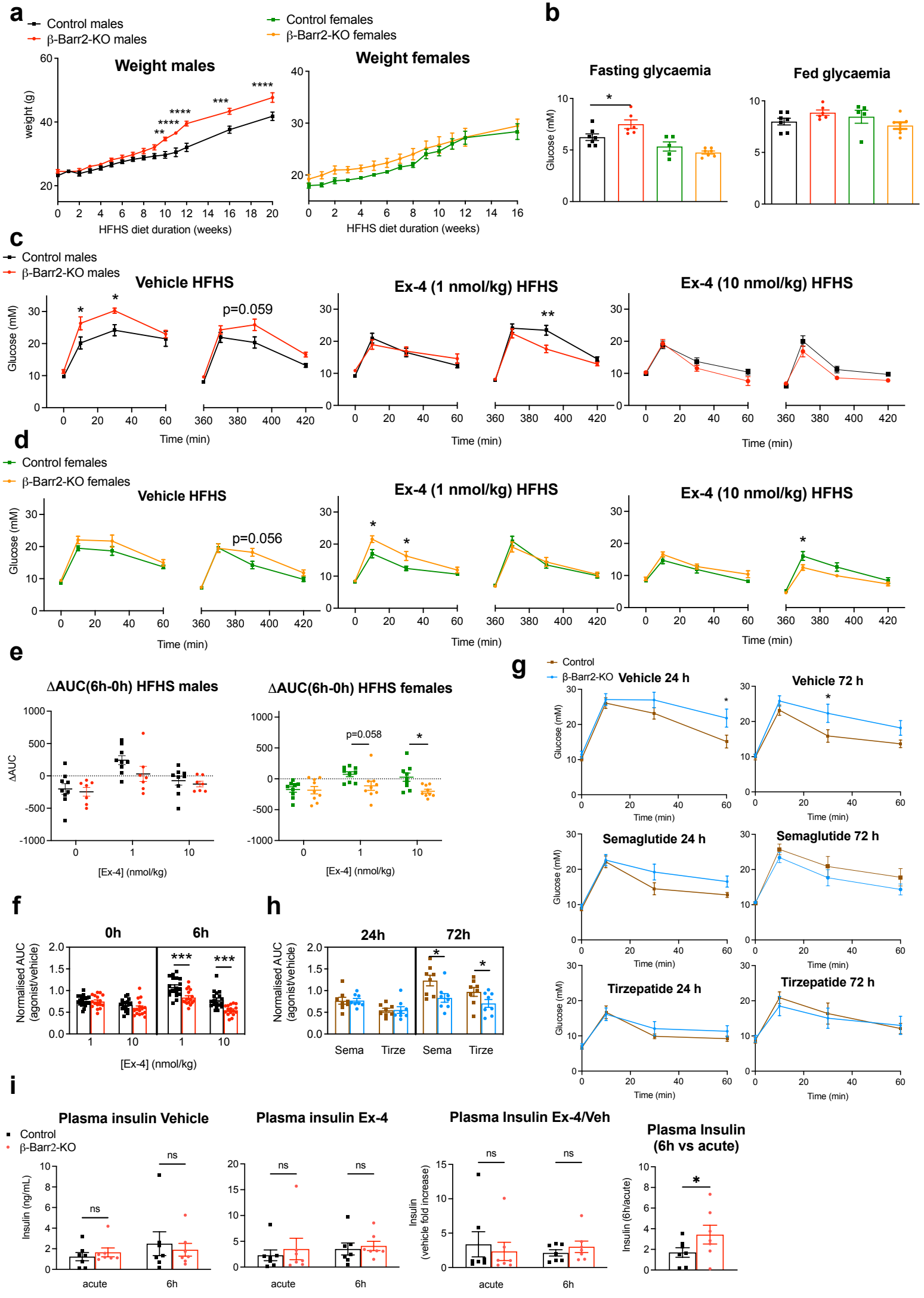
a
Control males
β-Barr2-KO males
Control females
β-Barr2-KO females
Weight males
weight (g)
HFHS diet duration (weeks)
Weight females
HFHS diet duration (weeks)
b
Fasting glycaemia
Glucose (mM)
Fed glycaemia
c
Control males
β-Barr2-KO males
Vehicle HFHS
Glucose (mM)
p=0.059
Ex-4 (1 nmol/kg) HFHS
Ex-4 (10 nmol/kg) HFHS
Time (min)
d
Control females
β-Barr2-KO females
Vehicle HFHS
Glucose (mM)
p=0.056
Ex-4 (1 nmol/kg) HFHS
Ex-4 (10 nmol/kg) HFHS
Time (min)
e
ΔAUC(6h-0h) HFHS males
ΔAUC(6h-0h) HFHS females
ΔAUC
p=0.058
[Ex-4] (nmol/kg)
f
0h
6h
Normalised AUC (agonist/vehicle)
[Ex-4] (nmol/kg)
h
24h
72h
Normalised AUC (agonist/vehicle)
Sema
Tirze
g
Control
β-Barr2-KO
Vehicle 24 h
Vehicle 72 h
Semaglutide 24 h
Semaglutide 72 h
Tirzepatide 24 h
Tirzepatide 72 h
Glucose (mM)
Time (min)
i
Plasma insulin Vehicle
Control
β-Barr2-KO
Insulin (ng/mL)
Plasma insulin Ex-4
Plasma Insulin Ex-4/Veh
Insulin (vehicle fold increase)
Plasma Insulin (6h vs acute)
Insulin (6h/acute)
ns
acute
6h

Figure 3

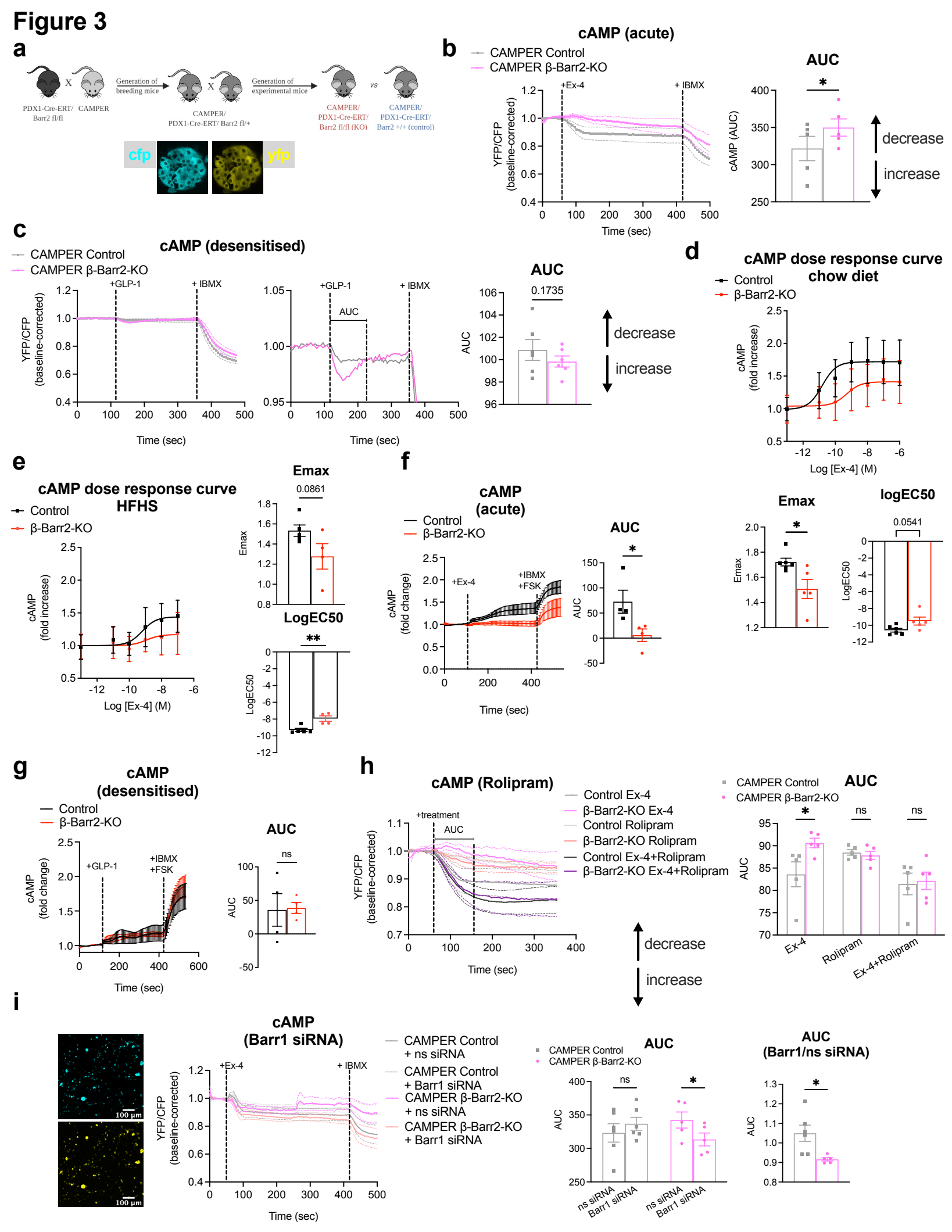
a
PDX1-Cre-ERT/ Barr2 fl/fl
CAMPER
Generation of breeding mice
CAMPER/ PDX1-Cre-ERT/ Barr2 fl/+
Generation of experimental mice
CAMPER/ PDX1-Cre-ERT/ Barr2 fl/fl (KO)
vs
CAMPER/ PDX1-Cre-ERT/ Barr2 +/+ (control)
cfp
yfp
b
cAMP (acute)
CAMPER Control
CAMPER β-Barr2-KO
+Ex-4
+ IBMX
YFP/CFP (baseline-corrected)
Time (sec)
AUC
cAMP (AUC)
decrease
increase
c
cAMP (desensitised)
CAMPER Control
CAMPER β-Barr2-KO
+GLP-1
+ IBMX
AUC
0.1735
d
cAMP dose response curve chow diet
Control
β-Barr2-KO
cAMP (fold increase)
Log [Ex-4] (M)
e
cAMP dose response curve HFHS
Emax
0.0861
LogEC50
f
cAMP (acute)
+IBMX +FSK
cAMP (fold change)
logEC50
0.0541
g
cAMP (desensitised)
ns
h
cAMP (Rolipram)
+treatment
Control Ex-4
β-Barr2-KO Ex-4
Control Rolipram
β-Barr2-KO Rolipram
Control Ex-4+Rolipram
β-Barr2-KO Ex-4+Rolipram
Ex-4
Rolipram
Ex-4+Rolipram
i
100 µm
cAMP (Barr1 siRNA)
CAMPER Control + ns siRNA
CAMPER Control + Barr1 siRNA
CAMPER β-Barr2-KO + ns siRNA
CAMPER β-Barr2-KO + Barr1 siRNA
ns siRNA
Barr1 siRNA
AUC (Barr1/ns siRNA)

Figure 4

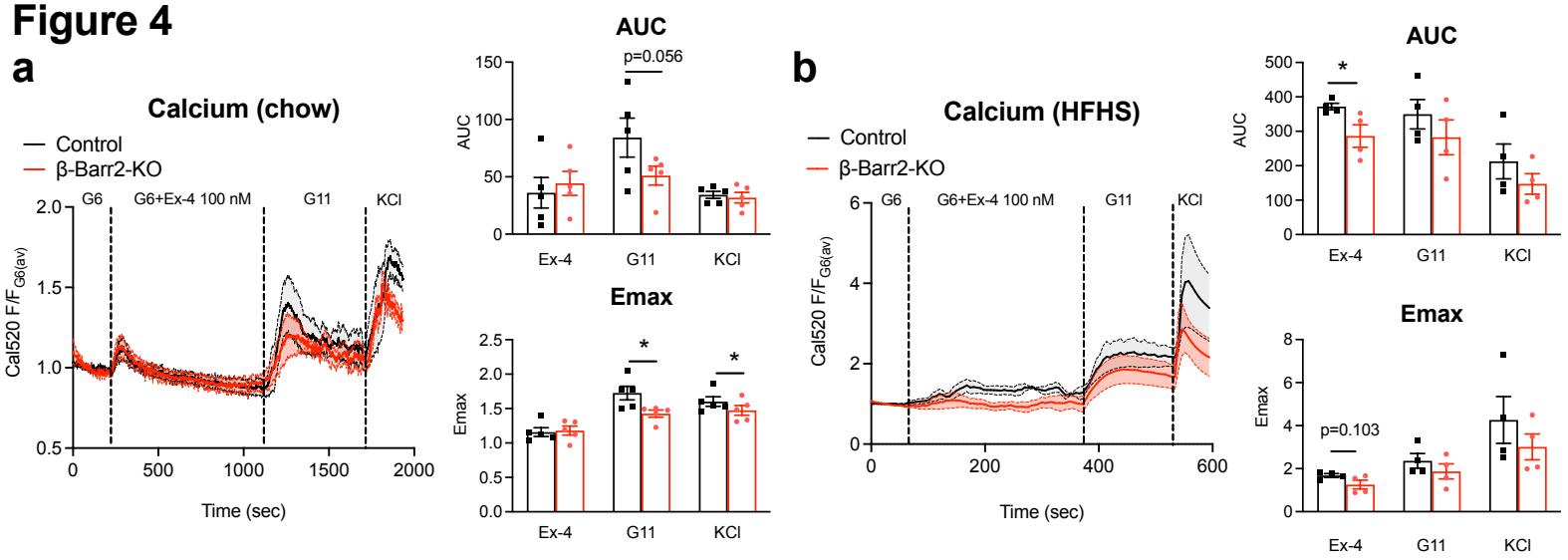
a
Calcium (chow)
Control
β-Barr2-KO
G6
G6+Ex-4 100 nM
G11
KCl
Cal520 F/F G6(av)
Time (sec)
AUC
p=0.056
Ex-4
G11
KCl
Emax
b
Calcium (HFHS)
Control
β-Barr2-KO
G6
G6+Ex-4 100 nM
G11
KCl
Cal520 F/F G6(av)
Time (sec)
AUC
Emax
p=0.103

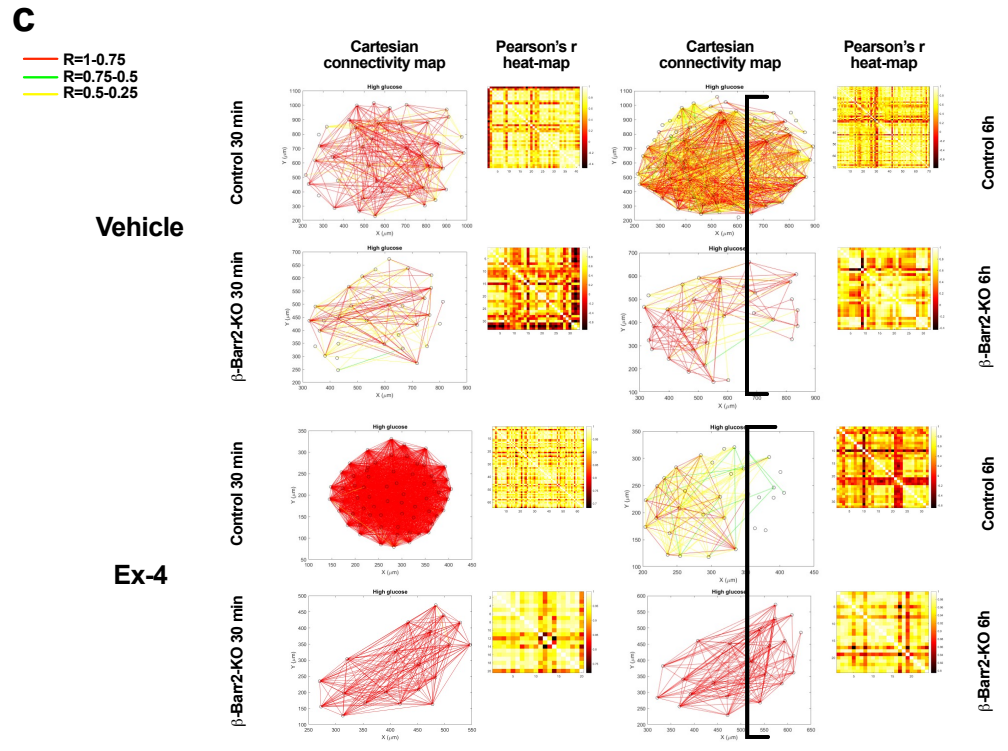
c
R=1-0.75
R=0.75-0.5
R=0.5-0.25
Cartesian connectivity map
Pearson's r heat-map
Cartesian connectivity map
Pearson's r heat-map
Vehicle
Ex-4
Control 30 min
β-Barr2-KO 30 min
Control 6h
β-Barr2-KO 6h

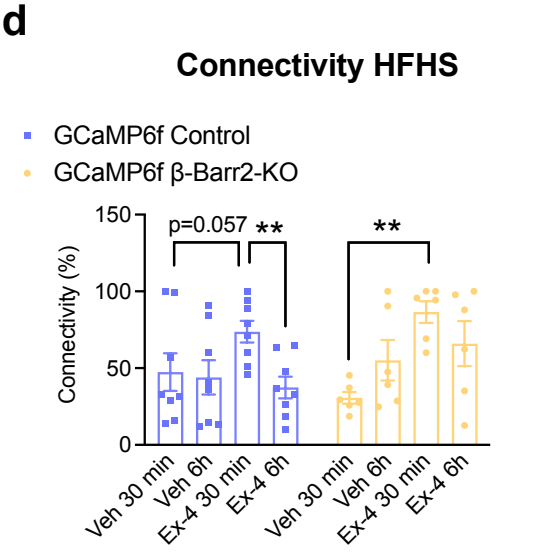
d
Connectivity HFHS
GCaMP6f Control
GCaMP6f β-Barr2-KO
Connectivity (%)
p=0.057
Veh 30 min
Veh 6h
Ex-4 30 min
Ex-4 6h

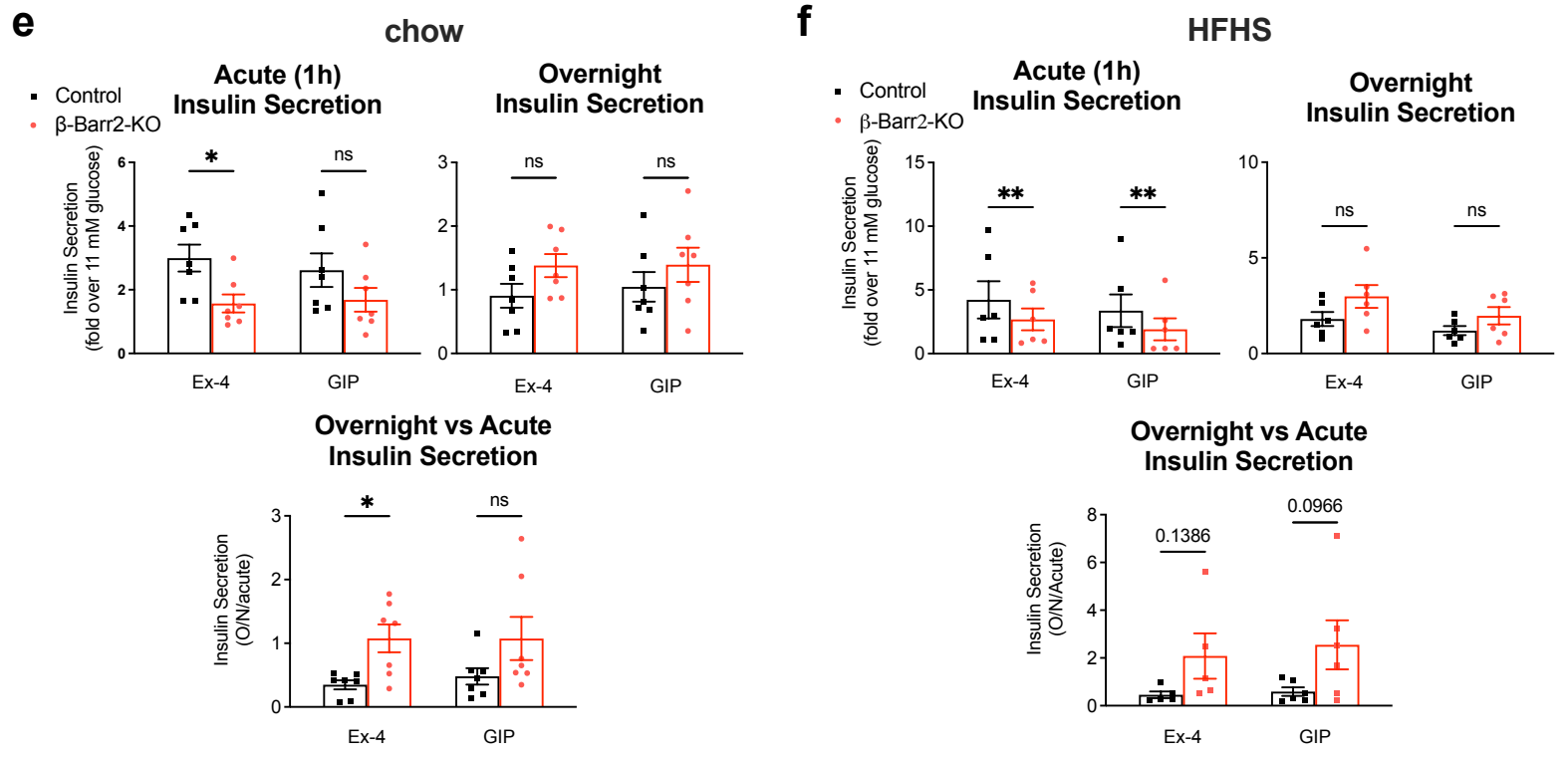
e
chow
Control
β-Barr2-KO
Acute (1h) Insulin Secretion
Overnight Insulin Secretion
Insulin Secretion (fold over 11 mM glucose)
Ex-4
GIP
Overnight vs Acute Insulin Secretion
Insulin Secretion (O/N/acute)
f
HFHS
Acute (1h) Insulin Secretion
Overnight Insulin Secretion
Overnight vs Acute Insulin Secretion
Insulin Secretion (O/N/Acute)
0.1386
0.0966

Figure 5

a

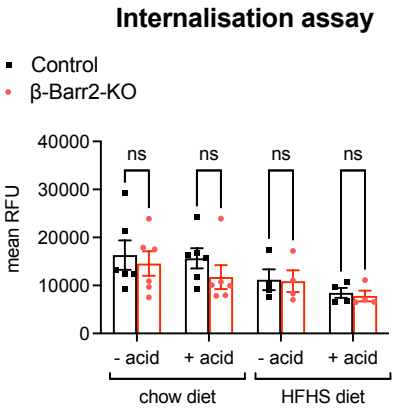

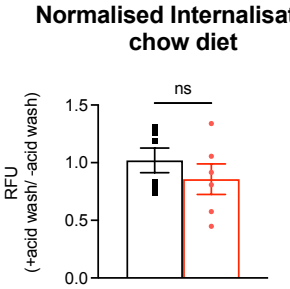

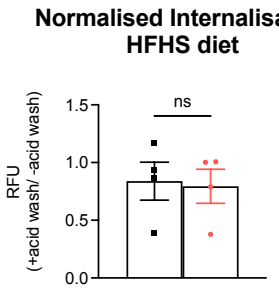

b

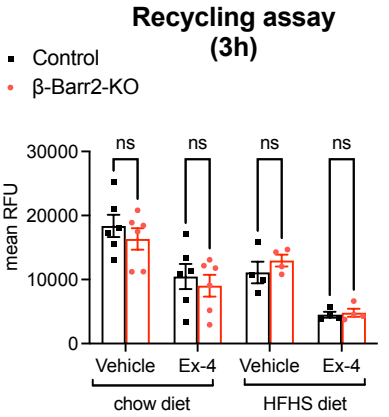

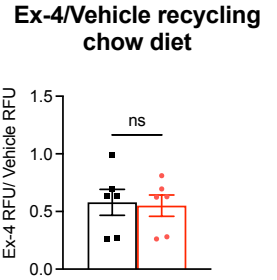

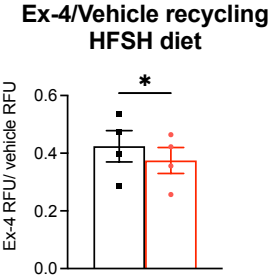

c

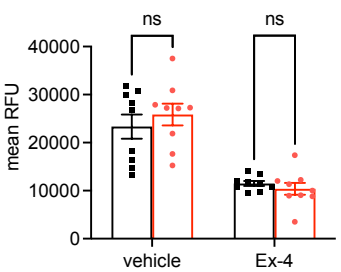

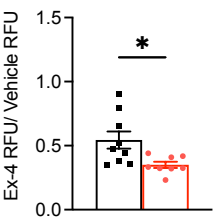

d

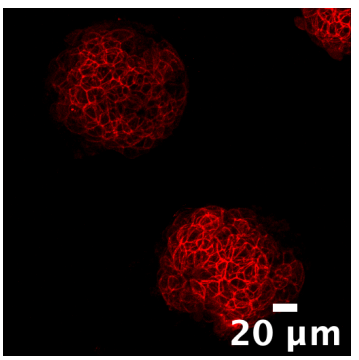

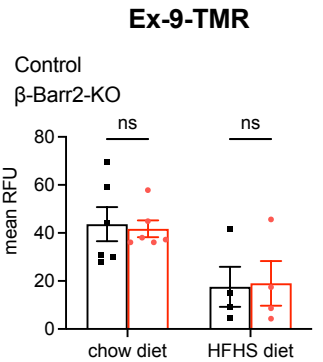

e

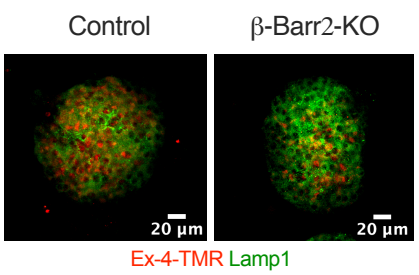

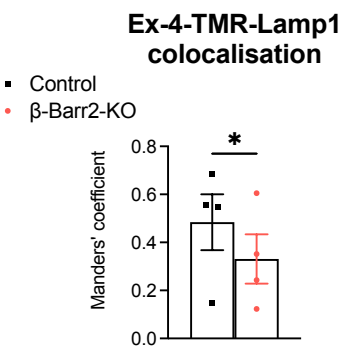

f

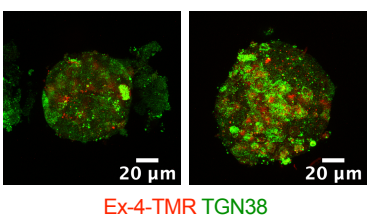

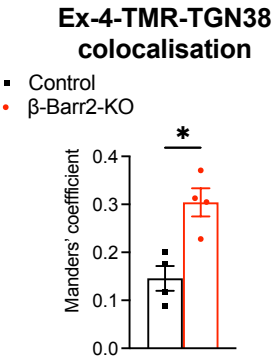

g

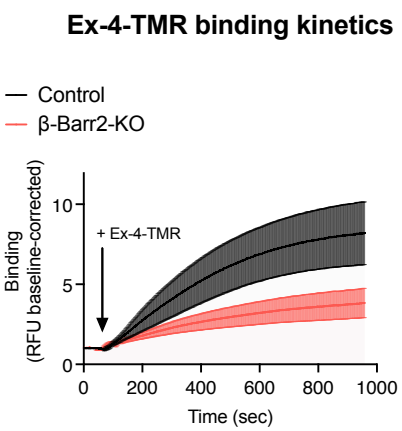

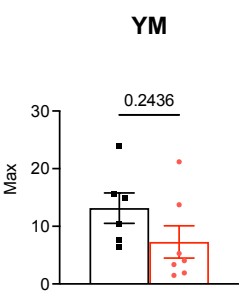

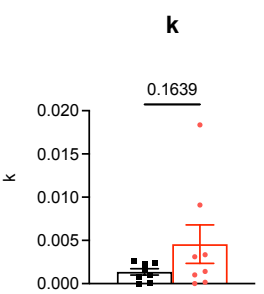

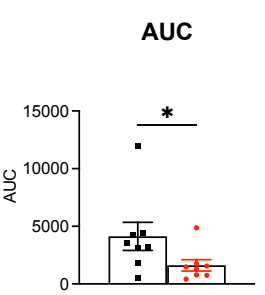

$$Y=YM-(YM-Y0)*\exp(-k*x)$$

Figure 6

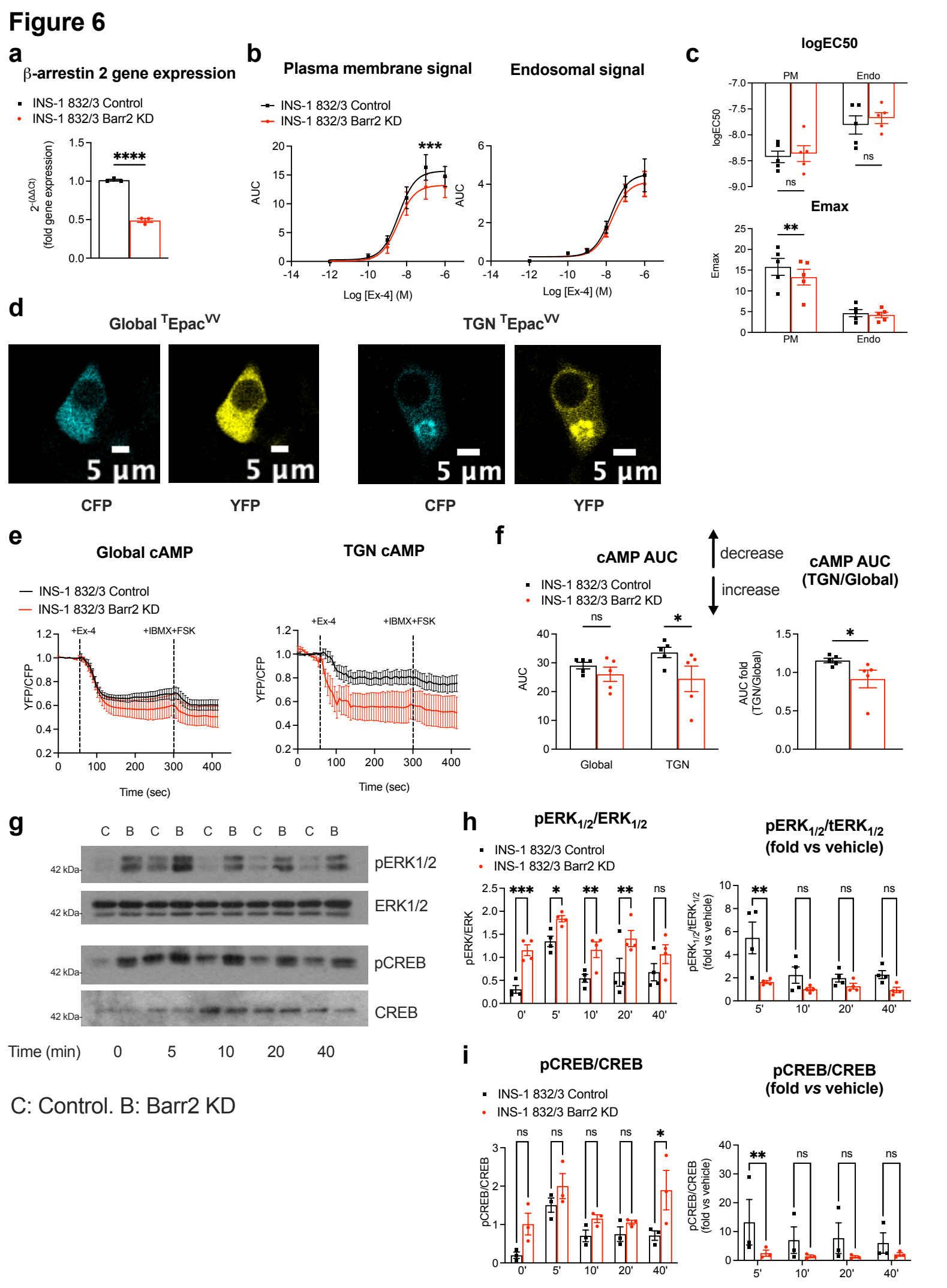
a
β-arrestin 2 gene expression
INS-1 832/3 Control
INS-1 832/3 Barr2 KD
2-(ΔΔct) (fold gene expression)
****
b
Plasma membrane signal
Endosomal signal
INS-1 832/3 Control
INS-1 832/3 Barr2 KD
AUC
***
Log [Ex-4] (M)
c
logEC50
PM
Endo
logEC50
ns
Emax
**
d
Global TEpacVV
TGN TEpacVV
5 µm
CFP
YFP
e
Global cAMP
TGN cAMP
INS-1 832/3 Control
INS-1 832/3 Barr2 KD
+Ex-4
+IBMX+FSK
YFP/CFP
Time (sec)
f
cAMP AUC
decrease
increase
cAMP AUC (TGN/Global)
INS-1 832/3 Control
INS-1 832/3 Barr2 KD
ns
*
AUC
Global
TGN
AUC fold (TGN/Global)
g
C B C B C B C B C B
42 kDa
pERK1/2
ERK1/2
pCREB
CREB
Time (min) 0 5 10 20 40
C: Control. B: Barr2 KD
h
pERK1/2/ERK1/2
INS-1 832/3 Control
INS-1 832/3 Barr2 KD
pERK/ERK
***
*
**
ns
0' 5' 10' 20' 40'
pERK1/2/tERK1/2 (fold vs vehicle)
i
pCREB/CREB
INS-1 832/3 Control
INS-1 832/3 Barr2 KD
pCREB/CREB
pCREB/CREB (fold vs vehicle)

Figure 7

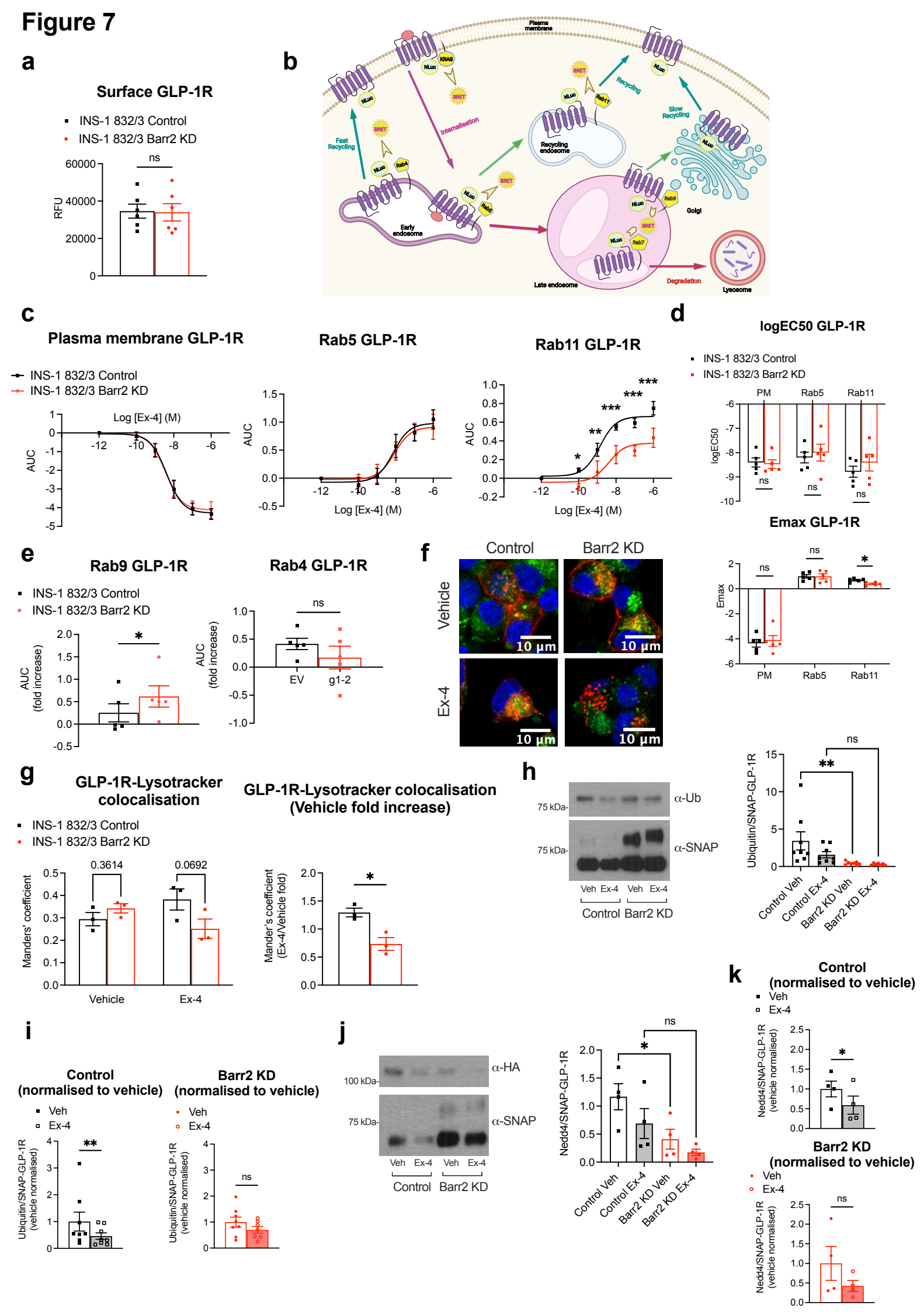
a
Surface GLP-1R
INS-1 832/3 Control
INS-1 832/3 Barr2 KD
RFU
ns
b
Plasma membrane
Internalisation
Fast Recycling
Slow Recycling
Recycling
Recycling endosome
Early endosome
Late endosome
Golgi
Degradation
Lysosome
BRET
NLuc
KRAS
Rab4
Rab5
Rab11
Rab9
Rab7
c
Plasma membrane GLP-1R
Rab5 GLP-1R
Rab11 GLP-1R
INS-1 832/3 Control
INS-1 832/3 Barr2 KD
Log [Ex-4] (M)
AUC
d
logEC50 GLP-1R
INS-1 832/3 Control
INS-1 832/3 Barr2 KD
PM
Rab5
Rab11
logEC50
ns
Emax GLP-1R
Emax
e
Rab9 GLP-1R
Rab4 GLP-1R
INS-1 832/3 Control
INS-1 832/3 Barr2 KD
AUC (fold increase)
EV
g1-2
f
Control
Barr2 KD
Vehicle
Ex-4
10 µm
g
GLP-1R-Lysotracker colocalisation
GLP-1R-Lysotracker colocalisation (Vehicle fold increase)
INS-1 832/3 Control
INS-1 832/3 Barr2 KD
Manders' coefficient
0.3614
0.0692
Vehicle
Ex-4
Mander's coefficient (Ex-4/Vehicle fold)
h
75 kDa
α-Ub
α-SNAP
Veh Ex-4 Veh Ex-4
Control Barr2 KD
Ubiquitin/SNAP-GLP-1R
Control Veh
Control Ex-4
Barr2 KD Veh
Barr2 KD Ex-4
i
Control (normalised to vehicle)
Barr2 KD (normalised to vehicle)
Veh
Ex-4
Ubiquitin/SNAP-GLP-1R (vehicle normalised)
j
100 kDa
75 kDa
α-HA
α-SNAP
Veh Ex-4 Veh Ex-4
Control Barr2 KD
Nedd4/SNAP-GLP-1R
Control Veh
Control Ex-4
Barr2 KD Veh
Barr2 KD Ex-4
k
Control (normalised to vehicle)
Barr2 KD (normalised to vehicle)
Veh
Ex-4
Nedd4/SNAP-GLP-1R (vehicle normalised)